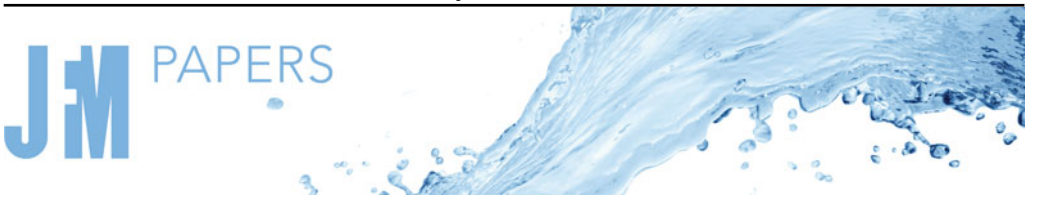
J. Fluid Mech. (2026), *vol.* 1030, A8, doi:10.1017/jfm.2026.11214



Stability analysis of transitional flows based on disturbance magnitude

Ofek Frank-Shapir[1] **and Igal Gluzman**[1]

[1]The Stephen B. Klein Faculty of Aerospace Engineering, Technion – Israel Institute of Technology, Haifa 32000, Israel

Corresponding author: Ofek Frank-Shapir, ofekfr@campus.technion.ac.il

(Received 1 July 2025; revised 4 December 2025; accepted 12 January 2026)

We propose a novel stability criterion for incompressible shear flows by combining input–output analysis and the small gain theorem. The criterion yields an explicit threshold on the magnitude of velocity perturbations about a given base flow that guarantees stability. If this threshold is crossed – either due to non-modal growth, exponential growth or a bypass transition scenario – our analysis predicts a loss of stability that may lead to transition to turbulence. We consider three approximated models for nonlinearity: unstructured, structured with non-repeated blocks and structured with repeated blocks. We show that the imposed threshold obtained by these three methods complies with a hierarchical relationship, where the unstructured case is the most conservative, imposing the lowest bound on disturbance magnitude. We apply this approach to three canonical and well-studied base flows: Couette, plane Poiseuille and Blasius. For these three base flows, we compare our results with experiments, direct numerical simulation results, non-modal nonlinear stability results and linear stability theory (LST). In the limit of infinitesimally small perturbation magnitude, our stability criterion for the unstructured case recovers the results of LST. For finite perturbations, the structured cases that account for nonlinear interactions provided stability thresholds that are consistent with experimental observations and simulation results of transition at both subcritical and post-critical Reynolds numbers for the considered base flows in our study. In particular, we utilise our stability criterion to demonstrate that Couette flow can become unstable and transition can be triggered at different Reynolds numbers, which is consistent with past experimental observations.

Key words: boundary layer stability, nonlinear instability, shear-flow instability

© The Author(s), 2026. Published by Cambridge University Press. This is an Open Access article, distributed under the terms of the Creative Commons Attribution licence (https://creativecommons.org/licenses/by/4.0/), which permits unrestricted re-use, distribution and reproduction, provided the original article is properly cited.

https://doi.org/10.1017/jfm.2026.11214 Published online by Cambridge University Press

1. Introduction

In transitional flow stability studies, two main approaches are typically considered. (i) Modal analysis (Taira *et al.* 2020) – which has been a leading approach in formulating linear stability theory (LST). This approach focuses on eigenvalue analysis of the flow response to initial conditions and involves infinitesimally small disturbances superimposed on a base flow. In LST, stability is defined in the infinite horizon sense, while disregarding short-time perturbation dynamics (Schmid 2007) and the effect of perturbation magnitude on flow stability. (ii) Non-modal analysis – which allows focusing on the response to external forcing and the study of flow behaviour in the finite horizon sense, such as the study of transient growth due to the non-normality of the linearised Navier–Stokes (LNS) operator (Schmid 2007; Karp & Cohen 2017; Lozano-Durán *et al.* 2021). In particular, in a non-modal approach using an input–output formulation, the governing equations are formulated as state equations. This allows for the computation of the system's frequency response, which contains a great deal of information and enables a detailed analysis of the response to external forcing. One field that employs such methodology is resolvent analysis (Schmid 2007; McKeon & Sharma 2010; McKeon 2017; Jovanović 2021). In these studies, the resolvent operator is formulated to examine the input–output dynamical response of the linearised system to harmonic forcing about a certain base flow via associated resolvent modes. The main difference between input–output works and resolvent analysis is that in resolvent analysis, the input–output dynamics is transformed into analyses of the resolvent modes, via a Schmidt decomposition of the transfer operator, taking a singular value associated with the particular input–output mode pair. In this way, the analyses of the input–output dynamics are transformed into analyses of the resolvent modes and the associated energy amplification. In the current study we place less emphasis on specific mode shapes and focus on amplification characteristics over a range of wavenumbers. This type of analysis aligns more with previous input–output works (Jovanovic & Bamieh 2001; Jovanović & Bamieh 2005; Liu & Gayme 2021). Such tools have been shown to be computationally efficient in providing insights into the response of different base flows to actuation. Examples include studies that focused on the externally forced LNS equations to examine dynamic processes, structural features and energy pathways for a variety of base flows (Farrell & Ioannou 1993; Bamieh & Dahleh 2001; Jovanović & Bamieh 2004, 2005; Hwang & Cossu 2010*a*; McKeon & Sharma 2010; McKeon, Sharma & Jacobi 2013; McKeon 2017; Madhusudanan, Illingworth & Marusic 2019; Liu & Gayme 2020*a*; Symon, Illingworth & Marusic 2021). Additional examples include our recent studies, where the dynamics of large-scale structures in a turbulent boundary layer are studied by analysing the flow response to external periodic perturbations (Liu *et al.* 2022) and utilisation of the input–output approach for modelling different actuation geometry patterns (Gluzman & Gayme 2021; Frank-Shapir & Gluzman 2025).

In Schmid (2007), it was stated: 'despite these remarkable accomplishments, many questions were left unanswered, including the discrepancy between the computed critical Reynolds number and the observed transitional Reynolds number in many wall-bounded shear flows, the interplay between linear energy amplification and nonlinear energy conservation in the subcritical regime, the nonexistence of finite critical Reynolds numbers for pipe or plane Couette flow, and a frequent failure to observe theoretically predicted structures in unforced experiments'. Many of these issues highlighted by Schmid (2007) continue to be valid nowadays. In particular, this study focuses on addressing the discrepancies between modal and non-modal approaches for identifying the governing flow structures responsible for the onset of instability and predicting the critical Reynolds number, which we review in detail next.

https://doi.org/10.1017/jfm.2026.11214 Published online by Cambridge University Press

Linear non-modal analysis methods, such as linear input–output analysis (Jovanović & Bamieh 2005), emphasise different predictions about the dominant flow structures. Classical results from linear modal stability analysis predict the prevalence of Tollmien–Schlichting (TS) waves as the modes that cause the loss of stability in shear flows. On the other hand, linear non-modal analysis emphasises streaky structures that are linked to the transient growth process (Reddy & Henningson 1993; Schmid & Henningson 1994; Schmid 2000; Bamieh & Dahleh 2001; Jovanovic 2004; Jovanović & Bamieh 2004, 2005; Schmid 2007). Both approaches are validated via experimental observations and numerical simulations, where TS waves are observed to lead to transition when the inflow is hardly noisy (Klebanoff, Tidstrom & Sargent 1962; Laurien & Kleiser 1989; Rist & Fasel 1995), and streaky structures lead to transition when the input boundary layer is noisy (Roach & Brierley 1989; Jacobs & Durbin 2001; Hernon, Walsh & McEligot 2007).

When considering the critical Reynolds number, one key result of LST is that Couette flow is stable for all Reynolds numbers (Romanov 1973). However, experimental evidence (Tillmark & Alfredsson 1992; Dauchot & Daviaud 1995), stochastic viewpoint at stability theory (Ko, Lucor & Sagaut 2011) and simulation results (Barkley & Tuckerman 2005; Dou & Khoo 2012) have observed transition in Couette flow at different Reynolds numbers, typically occurring in the range $Re = 320-370$. The same holds for other flow geometries (e.g. plane Couette–Poiseuille, plane Poiseuille and Blasius flows), for which there is plentiful literature, where instability is observed at subcritical Reynolds numbers (Nishioka & Asai 1985; Asai & Nishioka 1995; Burin & Czarnocki 2012; Chefranov & Chefranov 2016; Sano & Tamai 2016; Klotz *et al.* 2017; Huang *et al.* 2024) or remained stable even at post-critical Reynolds numbers (e.g. Pfenninger 1961; Nishioka *et al.* 1975; Avila, Barkley & Hof 2023). This disagreement of linear analysis methods with experimental and simulation results can be attributed to the omission of finite-size disturbances and nonlinear interactions in the stability analysis methods (Mullin 2010) that are evident from experiments (e.g. Cohen, Philip & Ben-Dov 2009; Sano & Tamai 2016) and direct numerical simulations (DNS) (e.g. He & Seddighi 2015).

Different approaches can be considered to represent the nonlinear advection term in the Navier–Stokes equations (NSE) and account for finite-size perturbations. Examples include using quadratic constraints and employing linear matrix inequalities to compute bounds on permissible perturbation magnitudes, ensuring the flow field remains laminar (Kalur, Seiler & Hemati 2020, 2021*a*,*b*; Liu & Gayme 2020*b*; Heide & Hemati 2025). In addition, optimal perturbation analysis using non-modal nonlinear methods (e.g. Duguet *et al.* 2013; Kerswell 2018; Parente *et al.* 2022) successfully addresses many shortcomings of linear analysis methods. These non-modal nonlinear approaches are based on computing the evolution of the entire flow field and optimising over the initial conditions. This process is very numerically demanding, limiting the ability of such works to study the effect of many perturbation magnitudes for a wide range of Reynolds numbers and wavenumbers. The framework proposed in this work for flow stability analysis is based on computing frequency response operators within an input–output paradigm rather than simulating the entire flow-field evolution. This makes our approach more computationally efficient than adjoint-based methods, allowing us to examine large ranges of Reynolds numbers, revealing the complex interplay between dominant flow structures that determine the stability threshold. In particular, we want to emphasise the study of Liu & Gayme (2021), where the authors proposed to recover the key flow features that are associated with nonlinear effects in input–output formulation by using the concept of structured uncertainty (Packard & Doyle 1993; Zhou, Doyle & Glover 1995) from the field of robust control theory. This approach is denoted as structured input–output analysis, in which the

https://doi.org/10.1017/jfm.2026.11214 Published online by Cambridge University Press

nonlinear term in the NSE is modelled as a fixed structure uncertainty that is interconnected to the linear frequency response operator obtained from the LNS equations. Different structures for the uncertainty are proposed in this and subsequent studies: repeated block uncertainty (Bhattacharjee *et al.* 2023; Mushtaq *et al.* 2023; Mushtaq *et al.* 2024) and non-repeated block uncertainty (Liu & Gayme 2021; Shuai, Liu & Gayme 2023) to incorporate the nonlinearity into the system. Within the proposed structured input–output formulation, the small gain theorem is used to define the stability of a structured feedback interconnection. This theorem is also used in Jovanovic (2004) to show that the robust stability analysis is equivalent to the input–output analysis for a certain part of the system.

This study builds upon the mentioned studies above, where we utilise input–output analysis and the small gain theorem to derive disturbance-based criteria for analysing the stability of flows. In our framework, we rewrite the LNS equations as a state-space based on the work of Jovanović & Bamieh (2005). Next, the framework is expanded to incorporate nonlinear interactions by introducing an uncertainty block, using structured input–output analysis (Liu & Gayme 2021; Mushtaq *et al.* 2023). This formulation is used to derive disturbance-based criteria for analysing the stability of the flows. This is achieved by relating the inverse of the largest structured singular value (SSV) to the magnitude of velocity perturbations in the flow, and utilising the small gain theorem to establish a threshold on velocity disturbance magnitude that triggers flow instability. We conduct a detailed study of applying this criterion to three canonical flows that are fundamental in stability studies, over a wide range of Reynolds numbers. In detail, we propose a novel stability analysis approach, based on determining a threshold on the disturbance magnitude present in the flow that triggers instability rather than examining the growth rate of modes in the flow through linear stability analysis. The threshold criterion provides an upper bound on the magnitude of velocity perturbations that ensures stability. This threshold can be reached via different bypass transition routes, such as through the existence of a finite-size perturbation in the flow (like in noisy environments and realistic experimental conditions) or via a transient growth scenario where a set of infinitesimal perturbations leads to a perturbation amplitude amplification that can surpass the estimated threshold by our approach. Therefore, our criterion can be applied to study a wide range of physical routes to transition.

In § 2 we provide a mathematical framework to formulate the stability criterion with details on numerical implementation, suitable for high-order flow models, provided in § 3. We use this criterion to analyse the transition of Couette, plane Poiseuille and Blasius flows for a wide range of Reynolds numbers. For each base flow, we consider three input–output formulations: unstructured input–output, structured input–output with non-repeating uncertainty and structured input–output with repeating uncertainty. We demonstrate that our threshold would comply with a hierarchical relationship, where the unstructured case is most conservative, imposing the lowest bound for transition, whereas structured cases are closer to the true value, by accounting for nonlinearity. In § 4 we also identify the dominant structures in transitional flows that determine the stability threshold bound for a wide range of Reynolds numbers and show a complex interplay between the structures that set the stability threshold in subcritical, near-critical and post-critical Reynolds number ranges.

We demonstrate that our criterion allows us to address the issues mentioned in Schmid (2007), regarding the discrepancy in transitional Reynolds number in many wall-bounded shear flows, and the dominant flow structures that govern different stages of transition. As detailed in § 5, our stability approach is in agreement with previous experimental works, which found that finite-amplitude perturbations can cause transition, and the critical amplitude depends on the Reynolds number (Dauchot & Daviaud 1995; Peixinho & Mullin 2007; Philip, Svizher & Cohen 2007). We also use the analysis presented in this paper to obtain stability diagrams, compare them to stability diagrams from LST and compute the

https://doi.org/10.1017/jfm.2026.11214 Published online by Cambridge University Press

critical perturbation energy required to cause flow instability, which shows a good agreement with DNS and non-modal nonlinear approaches (Reddy *et al.* 1998; Duguet *et al.* 2010*a*, 2013; Parente *et al.* 2022). Similar to other works using non-modal approaches, our novel stability criterion overcomes a shortcoming of LST, which shows the non-existence of a finite critical Reynolds number for plane Couette flow. We use our novel stability criterion to show that Couette flow is indeed unstable and can transition to turbulence at various Reynolds numbers, as supported by experimental results (Nishioka & Asai 1985; Burin & Czarnocki 2012; Klotz *et al.* 2017). Lastly, conclusions are discussed in § 6.

2. Theoretical background

We consider incompressible shear flow, for which the LNS equations for perturbations in fluid velocity and pressure $(\boldsymbol{u}, p)$ about the base flow $(\overline{\boldsymbol{u}}, \overline{p})$ are as follows:

$$\begin{gathered}\frac{\partial \boldsymbol{u}}{\partial t} = -\bar{\boldsymbol{u}} \cdot \nabla \boldsymbol{u} - \boldsymbol{u} \cdot \nabla \bar{\boldsymbol{u}} - \nabla p + \frac{1}{Re}\Delta \boldsymbol{u} + \boldsymbol{d}, \\ \nabla \cdot \boldsymbol{u} = 0.\end{gathered} \tag{2.1}$$

Here, $\boldsymbol{u} = \begin{bmatrix} u & v & w \end{bmatrix}^T$ is the perturbation velocity vector, corresponding to the streamwise x, wall-normal y and spanwise z directions, respectively. Throughout this work, we consider base velocity profiles of the form $\bar{\boldsymbol{u}} = \begin{bmatrix} U(y) & 0 & 0 \end{bmatrix}^T$. Additionally, $\boldsymbol{d} = \begin{bmatrix} d_x & d_y & d_z \end{bmatrix}^T$ is the term representing body forcing, ∇ is the del operator and $\Delta \equiv \nabla^2$ is the Laplacian operator.

In addition, we assume spatial invariance of the parallel flow field in the horizontal directions to allow Fourier transforms in the x and z directions, providing a system of two partial differential equations depending on spatial wavenumbers k_x, k_z and y, the position in the wall-normal direction (Kim, Moin & Moser 1987). Such an assumption is valid for Couette, plane Poiseuille and Blasius flow under a quasi-parallel assumption. This process allows us to write the LNS equations in a state-space form, which simplifies performing input–output analysis, via a formulation we adopt from Jovanović & Bamieh (2005):

$$\begin{gathered}\frac{\partial \boldsymbol{\psi}}{\partial t}(k_x, y, k_z, t) = [\mathscr{A}(k_x, k_z)\boldsymbol{\psi}(k_x, k_z, t)](y) + [\mathscr{B}(k_x, k_z)\boldsymbol{d}(k_x, k_z, t)](y), \\ \boldsymbol{\phi}(k_x, y, k_z, t) = [\mathscr{C}(k_x, k_z)\boldsymbol{\psi}(k_x, k_z, t)](y).\end{gathered} \tag{2.2}$$

Here $\boldsymbol{\psi} \equiv \begin{bmatrix} v & \omega_y \end{bmatrix}^T$ is the state vector, comprised of the wall-normal velocity perturbation v and the wall-normal vorticity perturbation $\omega_y = \partial u/\partial z - \partial w/\partial x$. The output vector $\boldsymbol{\phi}$ in our analysis is set to be $\boldsymbol{\phi} \equiv \boldsymbol{u} = \begin{bmatrix} u & v & w \end{bmatrix}^T$. Lastly, $\boldsymbol{d}$ is the body forcing term applied to the flow system. The operators denoted as $\mathscr{A}$, $\mathscr{B}$ and $\mathscr{C}$ are defined as (Jovanović & Bamieh 2005)

$$\mathscr{A} \equiv \begin{bmatrix} \mathscr{A}_{11} & 0 \\ \mathscr{A}_{21} & \mathscr{A}_{22} \end{bmatrix} \equiv \begin{bmatrix} -ik_x\Delta^{-1}U\Delta + ik_x\Delta^{-1}U'' + \dfrac{1}{Re}\Delta^{-1}\Delta^2 & 0 \\ -ik_zU' & -ik_xU + \dfrac{1}{Re}\Delta \end{bmatrix}, \tag{2.3}$$

$$\mathscr{B} \equiv \begin{bmatrix} \mathscr{B}_x & \mathscr{B}_y & \mathscr{B}_z \end{bmatrix} \equiv \begin{bmatrix} \Delta^{-1} & 0 \\ 0 & I \end{bmatrix} \begin{bmatrix} -ik_x\dfrac{\partial}{\partial y} & -\left(k_x^2 + k_z^2\right) & -ik_z\dfrac{\partial}{\partial y} \\ ik_z & 0 & -ik_x \end{bmatrix}, \tag{2.4}$$

https://doi.org/10.1017/jfm.2026.11214 Published online by Cambridge University Press

$$\mathscr{C} \equiv \begin{bmatrix} \mathscr{C}_u \\ \mathscr{C}_v \\ \mathscr{C}_w \end{bmatrix} \equiv \frac{1}{k_x^2 + k_z^2} \begin{bmatrix} ik_x \dfrac{\partial}{\partial y} & -ik_z \\ k_x^2 + k_z^2 & 0 \\ ik_z \dfrac{\partial}{\partial y} & ik_x \end{bmatrix}, \tag{2.5}$$

where $U' = \mathrm{d}U(y)/\mathrm{d}y$ and $U'' = d^2U(y)/\mathrm{d}y^2$. The Laplacian operator is defined as $\Delta = (\partial^2/\partial y^2) - (k_x^2 + k_z^2)$ because of the Fourier transforms done in directions x and z. Here $\mathscr{A}$ is the operator representing the dynamics of the system and is comprised of the Orr–Sommerfeld operator ($\mathscr{A}_{11}$), the coupling operator ($\mathscr{A}_{21}$) and the Squire operator ($\mathscr{A}_{22}$); $\mathscr{B}$ is the forcing operator, representing the effect of forcing input on the flow; $\mathscr{C}$ is the operator relating the state variables – wall-normal velocity and vorticity perturbations – to the three velocity perturbations (u, v, w). We note that the operator $\mathscr{C}$ can be modified to acquire the desired flow variables of interest as output of the system. Each of the operators $\mathscr{A}$, $\mathscr{B}$ and $\mathscr{C}$ implicitly depends on the wall-normal coordinate y.

Herein, the boundary conditions on v and ω_y depend on the specific base flow. For Couette and plane Poiseuille flows, the boundary conditions are

$$v(y = \pm 1) = \frac{\partial v}{\partial y}(y = \pm 1) = \omega_y(y = \pm 1) = 0, \quad \forall k_x, k_z \in \mathbb{R}, t \geqslant 0. \tag{2.6}$$

For Blasius base flow, the boundary conditions are

$$v(y = 0, \infty) = \frac{\partial v}{\partial y}(y = 0, \infty) = \omega_y(y = 0, \infty) = 0, \quad \forall k_x, k_z \in \mathbb{R}, t \geqslant 0. \tag{2.7}$$

Lastly, the Reynolds number is defined as $Re = \mathcal{U}L/\nu$, where $\mathcal{U}$ is the reference velocity, L is the reference height and ν is the kinematic viscosity of the fluid. These parameters are also used to render the variables in this work dimensionless. In particular, for Couette flow, $\mathcal{U}$ is half the difference between base flow velocity values at the lower and upper walls; for plane Poiseuille flow, it is the centreline velocity; for Blasius, it is the free-stream velocity. Here L is the channel half-height for both Couette and plane Poiseuille flows, and for Blasius flow, it is the displacement thickness.

2.1. *Linear frequency response*

In this section we consider the frequency response associated with the LNS system. The derivations in this section will be used as the foundation for the more complex nonlinear analysis, which we employ to obtain a stability criterion that is based on perturbation magnitude. Here, we consider a forcing term $\boldsymbol{d}$, which is harmonic in time and in the x and z directions, i.e. $\boldsymbol{d}(t, x, y, z) = \overline{\boldsymbol{d}}(y) \exp[i(k_x x + k_z z + \omega t)]$, where $\omega \in \mathbb{R}$ is the temporal frequency and $k_x, k_z \in \mathbb{R}$ are wavenumbers of the streamwise and spanwise flow directions, respectively, and $\overline{\boldsymbol{d}}(y)$ is some function of y, following the formulation in Jovanović & Bamieh (2005). In our study we do not consider any specific form of $\overline{\boldsymbol{d}}(y)$, instead the forcing component is viewed as the feedback in the interconnected system in figure 1 to account for the effect of the nonlinear advection term of the full NS system as will be detailed in § 2.3.

The frequency response operator that maps the harmonic forcing term applied to the state-space system in (2.2) to the resulting perturbation velocity field is given by (Zhou *et al.* 1995)

$$\mathscr{H}(y; k_x, k_z, \omega) = [\mathscr{C}(k_x, k_z)[i\omega \mathbf{I} - \mathscr{A}(k_x, k_z)]^{-1} \mathscr{B}(k_x, k_z)](y). \tag{2.8}$$

https://doi.org/10.1017/jfm.2026.11214 Published online by Cambridge University Press

Here, $\mathbf{I}$ is the identity matrix. As can be seen in (2.4) and (2.5), the operators $\mathscr{B}$ and $\mathscr{C}$ have three components each corresponding to different inputs and outputs, respectively.

The frequency response operator is used extensively in the input–output analysis of Jovanović & Bamieh (2005). Herein, we define an alternative operator, as proposed by Liu & Gayme (2021), and used in several structured input–output works (such as Mushtaq *et al.* 2023; Shuai *et al.* 2023):

$$\mathscr{H}_{\nabla}(y; k_x, k_z, \omega) \equiv \mathrm{diag}(\nabla, \nabla, \nabla)\mathscr{H}(y; k_x, k_z, \omega). \tag{2.9}$$

This frequency response operator of the system $\mathscr{H}_{\nabla}$ relates the forcing term to the resulting gradients of velocity perturbations. This operator will be useful for the derivation of a perturbation-based stability criterion that can incorporate nonlinear interactions via a structured input–output formulation, as will be shown in § 2.3.

2.2. *Choice of norms*

The selection of the norm plays a critical role in the analysis of input–output behaviours in flow systems. Norms serve as the mathematical infrastructure for quantifying the magnitude of the response to a specific input and provide a basis for defining and computing the amplification between an input and its corresponding output. It is important to note that different choices of norms are associated with the computation of different quantities. For example, the $\mathscr{H}_2$ norm is specifically used to represent perturbation kinetic energy, as referenced in Jovanović & Bamieh (2005). In our research, we utilise the $\mathscr{H}_\infty$ norm instead of the $\mathscr{H}_2$ norm, which is related to the amplification of one specific mode (which is the most amplified) in the flow, as shown next.

Given the operator $\mathscr{H}(y; k_x, k_z, \omega)$ after discretisation in y, we define the $\mathscr{H}_\infty$ system norm as (Zhou *et al.* 1995)

$$\|\mathscr{H}\|_\infty(k_x, k_z) \equiv \sup_{\omega\in\mathbb{R}} \overline{\sigma}[\mathscr{H}(k_x, k_z, \omega)], \tag{2.10}$$

and similarly,

$$\|\mathscr{H}_{\nabla}\|_\infty(k_x, k_z) \equiv \sup_{\omega\in\mathbb{R}} \overline{\sigma}[\mathscr{H}_{\nabla}(k_x, k_z, \omega)]. \tag{2.11}$$

Here, $\overline{\sigma}[\cdot]$ represents the largest singular value under the standard Euclidean inner product and $\sup_{\omega\in\mathbb{R}}$ represents the supremum operation over all temporal frequencies. Hence, the $\mathscr{H}_\infty$ norm does not quantify the energy amplification of the whole field, but rather the most amplified mode of the system due to harmonic temporal forcing.

2.3. *Nonlinear frequency response*

In this section we use structured input–output analysis to model the nonlinear response associated with the full NS system. This modelling of nonlinear interactions will be used in our stability analysis. We consider the full NS equations for velocity and pressure perturbations as we seek to incorporate nonlinear behaviours in our analysis. The NSE without a forcing term are as follows:

$$\begin{gathered}\frac{\partial \boldsymbol{u}}{\partial t} = -\bar{\boldsymbol{u}}\cdot\nabla\boldsymbol{u} - \boldsymbol{u}\cdot\nabla\bar{\boldsymbol{u}} - \nabla p + \frac{1}{Re}\Delta\boldsymbol{u} - \boldsymbol{u}\cdot\nabla\boldsymbol{u}, \\ \nabla\cdot\boldsymbol{u} = 0.\end{gathered} \tag{2.12}$$

Equation (2.12) is very similar to (2.1), with the only difference being that the forcing term is swapped by the nonlinear advection term $\boldsymbol{u}\cdot\nabla\boldsymbol{u}$. Thus, we can model nonlinear interactions as a forcing input to the LNS system. We model the nonlinear advection term

https://doi.org/10.1017/jfm.2026.11214 Published online by Cambridge University Press

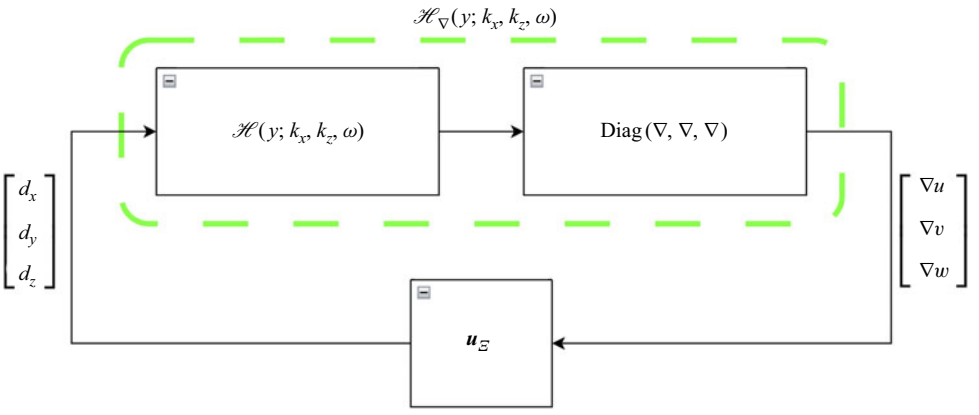


Figure 1. Interconnection loop block diagram for the nonlinear interactions. Adapted from Liu & Gayme (2021, figure 3).

in the NSE using the block diagram representation in figure 1. Here, $\boldsymbol{u}_\Xi$ is the gain applied to the vectorised velocity gradient $\begin{bmatrix}\nabla^T u & \nabla^T v & \nabla^T w\end{bmatrix}^T$ that retains the componentwise structure of the advection term $\boldsymbol{u}\cdot\boldsymbol{\nabla}\boldsymbol{u}$ (Liu & Gayme 2021). To interpret the feedback interconnection in figure 1 physically, we view the nonlinear advection term as an internal forcing mechanism acting on the LNS dynamics. In a standard 'unstructured' analysis, the feedback block $\boldsymbol{u}_\Xi$ is treated as a generic operator bounded only by its magnitude. Thus, unstructured analysis can be thought of as a worst case model of the nonlinearity, as there are no limitations on the individual terms in $\boldsymbol{u}_\Xi$. By contrast, the 'structured' feedback connection explicitly imposes constraints on $\boldsymbol{u}_\Xi$, such that the value of some of the terms in it is fixed to be zero. Structure constraints are imposed to limit feedback pathways for the goal of replicating the structure of the nonlinearity in the NSE (Liu & Gayme 2021). As will be shown in § 2.4, the unstructured analysis results in more conservative, lower bounds on velocity perturbations.

The exact expression for $\boldsymbol{u}_\Xi$ that captures the nature of the nonlinear term in the NSE is (see Liu & Gayme 2021, equation (2.9))

$$\boldsymbol{u}_\Xi \equiv \begin{bmatrix} -\boldsymbol{u}^T & \boldsymbol{0} & \boldsymbol{0} \\ \boldsymbol{0} & -\boldsymbol{u}^T & \boldsymbol{0} \\ \boldsymbol{0} & \boldsymbol{0} & -\boldsymbol{u}^T \end{bmatrix}. \tag{2.13}$$

For the rest of this work, we consider a discretised version of the operator $\boldsymbol{u}_\Xi$, which we denote as $\boldsymbol{U}_\Xi$. The discretisation in the wall-normal direction causes $\boldsymbol{U}_\Xi$ to be a constant-valued matrix. The exact expression for $\boldsymbol{U}_\Xi$ can be found in Appendix A. To incorporate this nonlinearity, we calculate SSVs of the system. The SSVs are a generalisation of the concept of singular values for the case of a transfer function or a frequency response operator that is feedback interconnected to an uncertain matrix, which has a predetermined structure (Zhou *et al.* 1995). In detail, similarly to the unstructured case, we calculate SSVs for the frequency response operator $\mathscr{H}_\nabla$ by solving the following minimisation problem (Packard & Doyle 1993; Zhou *et al.* 1995):

$$\mu_{\boldsymbol{\Delta}}[\mathscr{H}_\nabla(k_x, k_z, \omega)] = \frac{1}{min\{\overline{\sigma}(\boldsymbol{U}_\Xi) : \boldsymbol{U}_\Xi \in \boldsymbol{\Delta}, \det[I - \mathscr{H}_\nabla(k_x, k_z, \omega)\boldsymbol{U}_\Xi] = 0\}}. \tag{2.14}$$

In (2.14), $\overline{\sigma}(\cdot)$ represents the largest singular value, $\det[\cdot]$ is the determinant of a matrix and $\boldsymbol{\Delta}$ is a set of matrices that includes all the matrices that have a certain structure. Solving

https://doi.org/10.1017/jfm.2026.11214 Published online by Cambridge University Press

the SSV problem under the same (or similar) structure as $\boldsymbol{U}_{\varXi}$ allows modelling the 'worst case' nonlinear response to external velocity perturbations. In this framework, the matrix $\boldsymbol{U}_{\varXi}$ is not known *a priori*. Rather, it is computed by solving (2.14) such that the smallest structured uncertainty (in terms of the largest singular value) that will cause instability of the system. While in the current study $\boldsymbol{U}_{\varXi}$ models the nonlinear interactions, it is treated in the SSV framework as modelling uncertainty. Thus, we refer to $\boldsymbol{U}_{\varXi}$ for the rest of this work as the structured uncertainty. A detailed discussion about uncertainty structures is provided in § 2.5.

We quantify amplification with nonlinear interactions that are modelled by a structured uncertainty $\boldsymbol{U}_{\varXi} \in \boldsymbol{\Delta}$ using the supremum over all temporal frequencies, i.e.

$$\|\mathscr{H}\|_{\nabla\mu_{\boldsymbol{\Delta}}}(k_x, k_z) \equiv \sup_{\omega\in\mathbb{R}} \mu_{\boldsymbol{\Delta}}[\mathscr{H}_{\nabla}(k_x, k_z, \omega)], \tag{2.15}$$

this is the 'worst case' amplification of perturbation gradients under the uncertainty structure $\boldsymbol{\Delta}$. This amplification is not an amplification of the energy of the whole flow field, but rather the gain applied to the most amplified mode. Thus, we note that $\|\mathscr{H}_{\nabla}\|_{\mu_{\boldsymbol{\Delta}}}$ is a generalisation of $\|\mathscr{H}_{\nabla}\|_{\infty}$ for the case of interconnection of discretised $\mathscr{H}_{\nabla}$ with a structured uncertainty $\boldsymbol{U}_{\varXi}$. Additionally, we use the notation $\|\cdot\|_{\mu}$ for consistency with previous works (Packard & Doyle 1993; Liu & Gayme 2021), despite this operator not being a proper norm since it does not satisfy the triangle inequality.

2.4. *Small gain theorem formulation of stability*

In this section we use the small gain theorem to develop an understanding of the stability of flow systems represented by the NSE. This theorem is used to define the stability of structured feedback interconnections in the structured input–output formulation, providing stability margins for wall-bounded shear flows (Liu & Gayme 2021; Mushtaq *et al.* 2023, 2024; Shuai *et al.* 2023). Herein, we utilise the small gain theorem to establish a threshold on velocity disturbance magnitude that triggers flow instability. The interconnection in figure 1 is structured in a way compatible with the small gain theorem (see Zhou *et al.* 1995, Chapter 11), which for a fixed-in-time $\boldsymbol{U}_{\varXi}$ is phrased in the following manner.

THEOREM 1. *Suppose $\mathscr{H}_{\nabla}(k_x, k_z)$ is stable for a given wavenumber pair (k_x, k_z) and let $0 < \gamma < \infty$. The following is a sufficient condition for the feedback loop in figure 1 to be stable:*

$$\|\boldsymbol{U}_{\varXi}\|_{\infty} < 1/\gamma \tag{2.16}$$

if and only if

$$\|\mathscr{H}_{\nabla}\|_{\mu_{\boldsymbol{\Delta}}}(k_x, k_z) \leqslant \gamma. \tag{2.17}$$

Here, $1/\gamma$ constitutes a finite bound on $\|\boldsymbol{U}_{\varXi}\|_{\infty}$ and γ on $\|\mathscr{H}_{\nabla}\|_{\mu_{\boldsymbol{\Delta}}}$. Using singular value decomposition, it can be shown that (see Appendix A) $\|\boldsymbol{U}_{\varXi}\|_{\infty}$ is an approximation of the quantity $\max_{y\in\mathcal{Y}} \|\boldsymbol{u}(y)\|_2$ under the discretisation in the wall-normal direction. Here, $\mathcal{Y}$ is the relevant domain in the wall-normal direction corresponding to the flow system (for channel flows $\mathcal{Y} = [-1, 1]$, for boundary layer flows $\mathcal{Y} = [0, \infty)$); $\max_{y\in\mathcal{Y}} \|\boldsymbol{u}(y)\|_2$ denotes the largest velocity perturbation magnitude that is present in the flow. Combining equations (2.16) and (2.17) leads to the following condition for system stability:

$$\|\boldsymbol{U}_{\varXi}\|_{\infty} < \|\mathscr{H}_{\nabla}\|^{-1}_{\mu_{\boldsymbol{\Delta}}}(k_x, k_z). \tag{2.18}$$

https://doi.org/10.1017/jfm.2026.11214 Published online by Cambridge University Press

Therefore, (2.18) provides a bound of value $\|\mathscr{H}_{\nabla}\|^{-1}_{\mu_{\mathbf{\Delta}}}(k_x, k_z)$ on the magnitude of perturbations that are allowed in the flow to maintain stability. If the perturbation exceeds this bound, stability is no longer guaranteed and a transition to turbulence may occur. This formulation is capable of capturing the non-modal instability, i.e. transient growth mechanisms and flow instability triggered via bypass routes in the case of the presence of finite-size disturbances surpassing the threshold set by the small gain theorem criterion. Alternatively, for a given magnitude of external velocity perturbations, (2.18) can be used to bound the gain applied by the flow system, quantified by $\|\mathscr{H}_{\nabla}\|_{\mu_{\mathbf{\Delta}}}(k_x, k_z)$. This interpretation relates disturbance size and the magnitude of non-modal growth allowed in the flow. Following (2.18), the wavenumber pair that determines the stability threshold bound for a given Reynolds number can be defined as

$$\left[\left(k_x^*, k_z^*\right)_{\mu_{\mathbf{\Delta}}}\right](Re) \equiv \arg\min\left\{\left[\|\mathscr{H}_{\nabla}\|^{-1}_{\mu_{\mathbf{\Delta}}}(k_x, k_z)\right](Re)\right\}. \tag{2.19}$$

Here, we denote this mode as the most dominant mode for a particular Reynolds number that arises from our structured analysis. We note that in (2.17) in Theorem 1, the norm-like quantity $\|\mathscr{H}_{\nabla}\|_{\mu_{\mathbf{\Delta}}}$ can be replaced by $\|\mathscr{H}_{\nabla}\|_{\infty}$, representing a version of the small gain theorem in which the structure of the uncertainty is not considered (see Zhou *et al.* 1995, Chapter 9). This operation yields the following relation:

$$\|\boldsymbol{U}_{\Xi}\|_{\infty} < \|\mathscr{H}_{\nabla}\|^{-1}_{\infty}(k_x, k_z). \tag{2.20}$$

The use of $\|\mathscr{H}_{\nabla}\|_{\infty}$ instead of $\|\mathscr{H}_{\nabla}\|_{\mu_{\mathbf{\Delta}}}$ is equivalent to replacing the set Δ with the set of all complex-valued matrices of compatible size (Packard & Doyle 1993; Zhou *et al.* 1995; Liu & Gayme 2021), meaning that no particular feedback structure is considered. As denoted earlier, $\|\boldsymbol{U}_{\Xi}\|_{\infty}$ corresponds to the largest velocity perturbation magnitude (i.e. corresponds to $\max_{y\in\mathcal{Y}}\|\boldsymbol{u}(y)\|_2$) that is found in the flow. The inequality in (2.20) provides a stability criterion, which determines the maximal perturbation value allowed in the flow to guarantee the flow system stability.

Equivalently to the structured case, the most dominant mode for a given Reynolds number for the unstructured case can be defined as

$$\left[\left(k_x^*, k_z^*\right)_{\infty}\right](Re) \equiv \arg\min\left\{\left[\|\mathscr{H}_{\nabla}\|^{-1}_{\infty}(k_x, k_z)\right](Re)\right\}. \tag{2.21}$$

In general, we note that the following inequality always holds for any complex-valued matrix $\boldsymbol{M}$ and some set of matrices $\mathbf{\Delta}$ (Zhou *et al.* 1995):

$$\forall \mathbf{\Delta}, \boldsymbol{M} : \mu_{\mathbf{\Delta}}(\boldsymbol{M}) \leqslant \overline{\sigma}(\boldsymbol{M}). \tag{2.22}$$

By replacing $\boldsymbol{M}$ with $\mathscr{H}_{\nabla}$ and taking the supremum of both terms in (2.22), we obtain

$$\forall \mathbf{\Delta} : \|\mathscr{H}_{\nabla}\|_{\mu_{\mathbf{\Delta}}}(k_x, k_z) \leqslant \|\mathscr{H}_{\nabla}\|_{\infty}(k_x, k_z). \tag{2.23}$$

From (2.23) it follows that

$$\forall \mathbf{\Delta} : \|\mathscr{H}_{\nabla}\|^{-1}_{\mu_{\mathbf{\Delta}}}(k_x, k_z) \geqslant \|\mathscr{H}_{\nabla}\|^{-1}_{\infty}(k_x, k_z). \tag{2.24}$$

Both $\|\mathscr{H}_{\nabla}\|^{-1}_{\mu_{\mathbf{\Delta}}}$ and $\|\mathscr{H}_{\nabla}\|^{-1}_{\infty}$ are bounds on the magnitude of the maximal velocity perturbation via structured and unstructured approaches, respectively. Our approach provides a threshold on disturbance magnitude to trigger instability. In both (structured and unstructured) cases, the wavenumber domain is the same, allowing for the same disturbances to be considered in both cases. Here, the structured case is a subset of an unstructured case. This, in turn, implies that there are more amplification routes/scenarios for the unstructured case than for structured cases that consider only a subset of such scenarios, limited by the imposed structure on the gain block. The structured approach

https://doi.org/10.1017/jfm.2026.11214 Published online by Cambridge University Press

takes into account the structure of $\boldsymbol{U}_{\Xi}$ to model the physics of the nonlinear interactions that are an integral part of the realistic transitional flow physics. Therefore, we expect $\|\mathscr{H}_{\nabla}\|_{\mu_{\boldsymbol{\Delta}}}^{-1}$ to be a more representative criterion for stability, while $\|\mathscr{H}_{\nabla}\|_{\infty}^{-1}$ will be overly strict, and can predict lower bounds on velocity perturbation magnitude than what the actual flow allows.

2.5. *Structures of uncertainty*

In this section we discuss several possible structures for the structured uncertainty $\boldsymbol{U}_{\Xi}$, that are used for approximating the nonlinear term in the NSE and obtaining the best approximation to $\|\mathscr{H}_{\nabla}\|_{\mu_{\boldsymbol{\Delta}}}$. These structures arise after a suitable discretisation in the wall-normal direction is applied to the system. The uncertainty structure that approximates the product of $\boldsymbol{u}_{\Xi}$ and the vector of velocity perturbation gradient reproducing the structure of the advection term in the Navier–Stokes equation is

$$\boldsymbol{\Delta}_{\boldsymbol{u}} = \left\{ \begin{bmatrix} \Delta_u & \boldsymbol{0} & \boldsymbol{0} \\ \boldsymbol{0} & \Delta_u & \boldsymbol{0} \\ \boldsymbol{0} & \boldsymbol{0} & \Delta_u \end{bmatrix}, \Delta_u = [\mathrm{diag}(u_\xi), \mathrm{diag}(v_\xi), \mathrm{diag}(w_\xi)] : u_\xi, v_\xi, w_\xi \in \mathbb{C}^{N_y \times 1} \right\}, \tag{2.25}$$

where u_ξ, v_ξ, w_ξ can have complex entries because they represent Fourier-transformed velocity components; N_y is the number of points that are used in the discretisation of the wall-normal direction. Equation (2.25) represents the structure that arises after a discretisation of (2.13). This structure ensures that the feedback interconnection loop in figure 1 accurately recreates the structure of the nonlinear advection term. Any additional terms that are not included in the set $\boldsymbol{\Delta}_{\boldsymbol{u}}$ may be regarded as fictitious nonlinear interactions that are not part of the term $\boldsymbol{u} \cdot \nabla \boldsymbol{u}$ and, thus, do not represent physical flow behaviours.

The structure of the uncertainty should ideally be similar to $\boldsymbol{\Delta}_{\boldsymbol{u}}$ for an accurate model of the physics of nonlinear interactions. The solution for uncertainties in $\boldsymbol{\Delta}_{\boldsymbol{u}}$ involves the solution of the optimisation problem in (2.14) with a very complex set of constraints that are required for preserving the structure in (2.25). Such a solution has not yet been found, as far as we know. Alternatively, approximating this structure of the uncertainties is considered, which we detail next. In this work we use two different sets of matrices that are simpler in structure and are meant to approximate the uncertainty structure from (2.14). These sets are as follows.

(i) Set $\boldsymbol{\Delta}_r$: the set of block-diagonal matrices with three repeating full blocks with compatible sizes as was used in the works of Mushtaq *et al.* (2023, 2024),

$$\boldsymbol{\Delta}_r = \left\{ \begin{bmatrix} \Delta_r & \boldsymbol{0} & \boldsymbol{0} \\ \boldsymbol{0} & \Delta_r & \boldsymbol{0} \\ \boldsymbol{0} & \boldsymbol{0} & \Delta_r \end{bmatrix} : \Delta_r \in \mathbb{C}^{N_y \times 3N_y} \right\}. \tag{2.26}$$

Here, Δ_r can be any matrix of compatible dimensions ($N_y \times 3N_y$).

(ii) Set $\boldsymbol{\Delta}_{nr}$: the set of block-diagonal matrices with three full, independent non-repeating blocks with compatible sizes, as was used in the works of Liu & Gayme (2021), Shuai *et al.* (2023):

$$\boldsymbol{\Delta}_{nr} = \left\{ \begin{bmatrix} \Delta_1 & \boldsymbol{0} & \boldsymbol{0} \\ \boldsymbol{0} & \Delta_2 & \boldsymbol{0} \\ \boldsymbol{0} & \boldsymbol{0} & \Delta_3 \end{bmatrix} : \Delta_1, \Delta_2, \Delta_3 \in \mathbb{C}^{N_y \times 3N_y} \right\}. \tag{2.27}$$

https://doi.org/10.1017/jfm.2026.11214 Published online by Cambridge University Press

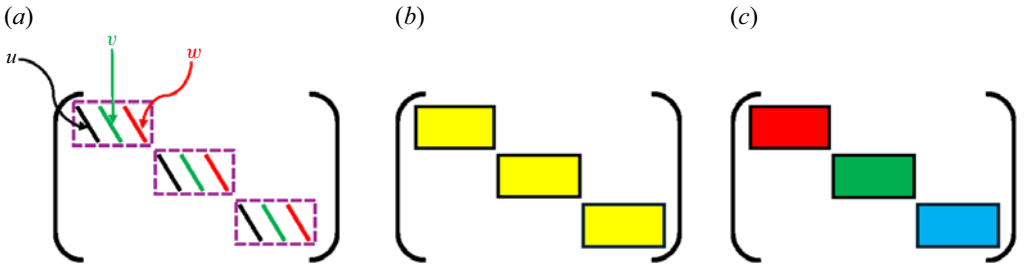


Figure 2. Illustration of uncertainty matrices with relevant structures: (*a*) uncertainty structure that is based on the feedback interconnection as defined in (2.25), (*b*) repeated block structure as defined in (2.26), (*c*) non-repeated block structure as defined in (2.27). Visualisations of the uncertainty matrices are shown for (*a*) $\boldsymbol{U}_\Xi \in \boldsymbol{\Delta}_{\boldsymbol{u}}$, (*b*) $\boldsymbol{U}_\Xi \in \boldsymbol{\Delta}_r$, (*c*) $\boldsymbol{U}_\Xi \in \boldsymbol{\Delta}_{nr}$.

The difference here between $\boldsymbol{\Delta}_{nr}$ and $\boldsymbol{\Delta}_r$ lies in the fact that $\boldsymbol{\Delta}_{nr}$ does not include the constraint of equal blocks, as Δ_1, Δ_2 and Δ_3 can be different matrices.

Visualisation of the uncertainty matrices that correspond to the structures $\boldsymbol{\Delta}_{\boldsymbol{u}}$, $\boldsymbol{\Delta}_r$ and $\boldsymbol{\Delta}_{nr}$ are illustrated in figure 2. We note that solving the minimisation problem for $\boldsymbol{\Delta}_r$ is computationally more demanding than for $\boldsymbol{\Delta}_{nr}$. While $\boldsymbol{\Delta}_{nr}$ imposes a single constraint on the uncertainty structure to be a set of block-diagonal matrices, $\boldsymbol{\Delta}_r$ imposes an additional constraint by requiring these blocks to be equal.

The definitions in (2.25), (2.26) and (2.27) yield

$$\boldsymbol{\Delta}_{\boldsymbol{u}} \subset \boldsymbol{\Delta}_r \subset \boldsymbol{\Delta}_{nr} \subset \mathbb{C}^{3N_y \times 9N_y}. \tag{2.28}$$

These relations between sets are manifested in the values of the SSVs for each set. Based on the monotonicity of the SSV with respect to set inclusion (see Scherer 2001, § 4.10), solving the minimisation problem (2.14) over these sets of matrices that satisfy the relations in (2.28), yields

$$\|\mathscr{H}_{\boldsymbol{\nabla}}\|_{\mu_{\boldsymbol{\Delta}_u}}(k_x, k_z) \leqslant \|\mathscr{H}_{\boldsymbol{\nabla}}\|_{\mu_{\boldsymbol{\Delta}_r}}(k_x, k_z) \leqslant \|\mathscr{H}_{\boldsymbol{\nabla}}\|_{\mu_{\boldsymbol{\Delta}_{nr}}}(k_x, k_z) \leqslant \|\mathscr{H}_{\boldsymbol{\nabla}}\|_{\infty}(k_x, k_z). \tag{2.29}$$

As we will show next, this hierarchical relationship allows us to explain the difference in the predictions of the most dominant mode by unstructured and structured input–output methods. Moreover, the norm-like property of the smallest set $\boldsymbol{\Delta}_{\boldsymbol{u}}$ is $\|\mathscr{H}_{\boldsymbol{\nabla}}\|_{\mu_{\boldsymbol{\Delta}_u}}(k_x, k_z)$, which inverse $(\|\mathscr{H}_{\boldsymbol{\nabla}}\|^{-1}_{\mu_{\boldsymbol{\Delta}_u}})$ would provide the least tight and most accurate bound to perturbation magnitude to keep the system stable. In particular, the inequality in (2.20) can serve as a generalised stability criterion, which is more physically justified to study pathways to transition, in contrast to classical stability theory, in which the mathematical formulation is restricted to infinitesimally small perturbations. However, as mentioned previously, the solution to such a set requires the solution of the optimisation problem in (2.14), which is elaborate and has not yet been found. The best next approximation of this set would be to use $\|\mathscr{H}_{\boldsymbol{\nabla}}\|^{-1}_{\mu_{\boldsymbol{\Delta}_r}}$, which is the most representing bound on velocity perturbation magnitude that we can compute, while $\|\mathscr{H}_{\boldsymbol{\nabla}}\|^{-1}_{\mu_{\boldsymbol{\Delta}_{nr}}}$ and $\|\mathscr{H}_{\boldsymbol{\nabla}}\|^{-1}_{\infty}$ provide more restricting bounds, respectively.

3. Numerical analysis settings

To compute the operators in (2.2) and the flow field they produce, we apply discretisation to the wall-normal direction by using Chebyshev collocation points. We implement

https://doi.org/10.1017/jfm.2026.11214 Published online by Cambridge University Press

this discretisation process by using the pseudo-spectral differentiation matrices from Weideman & Reddy (2000) for differentiation in the wall-normal direction. Boundary conditions were implemented based on Trefethen (2000). In particular, we employ a quasi-parallel assumption and use the change of variables described in Schmid, Henningson & Jankowski (2002) to transform the bounded domain $\left[-1,\ 1\right]$ to the semi-infinite domain $\left[0,\quad \infty\right]$ of the flat plate boundary layer (for details, see Schmid *et al.* 2002, Appendix A.4). We set the wall-normal domain range to $[0,\ L_y] = \left[0,\ 15\right]$ as this height is well within the free stream, capturing the entire base flow profile variation. We verified that the selected domain provides converged results, with no significant effect on the results in our study. Specifically, the maximum difference between the contour plots of the $\|\mathscr{H}_{\nabla}\|_{\infty}$ generated with increased domain $L = 20$ was less than 4 %.

All of the calculations are performed in MATLAB® R2023b. We denote by N_y the number of Chebyshev collocation points chosen for the discretisation process. For the wavenumber domain, we used a 50×90 grid of logarithmically spaced values with the following boundaries: ($k_{x_{min}} = 10^{-4}$, $k_{x_{max}} = 3.02$) and ($k_{z_{min}} = 10^{-2}$, $k_{z_{max}} = 15.84$). This is the same grid used in Jovanović & Bamieh (2005). A Chebyshev collocation method with $N_y = 61$ points was used for discretisation along the wall-normal direction in all computations and for all base flows. This spacing was determined to be adequate for obtaining reliable results, as doubling the number of source points did not affect the trends and values of the curves, nor did it cause any noticeable changes in the contour plots presented in § 4.

In terms of temporal frequencies, an adaptive approach was applied using MATLAB, utilising the highly computationally efficient *sigma* and *mussv* MATLAB functions. The results obtained from this adaptive method were compared with those obtained using a constant grid of frequency values. It was demonstrated that the results from the constant grid approach were converging to those achieved by adaptively selecting temporal frequencies.

The values of the $\mathscr{H}_{\infty}$ norm were calculated by using the MATLAB function *hinfnorm*, which is part of the robust control toolbox (Balas *et al.* 2005). Additionally, we calculate the estimated value of $\|\mathscr{H}_{\nabla}\|_{\mu}$ for the case of $\boldsymbol{U}_{\Xi} \in \boldsymbol{\Delta}_{nr}$ using the function *mussv* in the robust control toolbox (Balas *et al.* 2005), and we use the numerical algorithm of generalised power iteration for finding lower bounds on the SSV (Mushtaq *et al.* 2023) for the case of $\boldsymbol{U}_{\Xi} \in \boldsymbol{\Delta}_{r}$.

4. Effect of Reynolds number on disturbance threshold

This section presents a detailed analysis of the effect of the Reynolds number on disturbance threshold, and the dominant structures that determine the stability threshold bound for plane Couette, plane Poiseuille, and Blasius flows. For each base flow, we study the flow system stability characteristics using our stability criterion, which was derived in § 2.4 by evaluating the following.

(a) Structured norm-like quantities (and their inverse) defined in (2.15) using

  (i) repeated blocks approach, denoted as $\|\mathscr{H}_{\nabla}\|_{\mu_{\boldsymbol{\Delta}_r}}(k_x, k_z)$;
  (ii) non-repeated blocks approach, denoted as $\|\mathscr{H}_{\nabla}\|_{\mu_{\boldsymbol{\Delta}_{nr}}}(k_x, k_z)$.

(b) Unstructured linear norm, denoted as $\|\mathscr{H}_{\nabla}\|_{\infty}(k_x, k_z)$ in (2.11).

We examine and analyse here the contour plots of the quantities mentioned above over the k_x, k_z domain at specific Reynolds numbers. With this approach, we identify modes of

https://doi.org/10.1017/jfm.2026.11214 Published online by Cambridge University Press

	Couette	Plane Poiseuille	Blasius
DLR	(0.196, 0.628)	(1.561, 0.692)	(0.241, 0.274)
TS	(0.2, 10^{-2})	(1.02, 10^{-2})	(0.303, 10^{-2})
SPS	(10^{-4}, 1.436)	(10^{-4}, 1.841)	(10^{-4}, 0.274)
DHR	(0.01, 0.13)	(−)	(−)

Table 1. Selected modes (DLR - dominant low Reynolds, TS - Tollmien–Schlichting, SPS - spanwise periodic streak, DHR - dominant high Reynolds) for each base flow, represented by a pair of wavenumbers (k_x, k_z).

interest that determine the stability threshold bound in our analysis. Next, we analyse the behaviour of preselected (three to four) modes across a wide range of Reynolds numbers that we identified as dominant modes that emerged during the system excitation of each base flow. We focus on several specific modes since it would not be feasible to determine the most dominant mode (k_x^*, k_z^*) – that determines the stability threshold bound – and the corresponding stability threshold for the above norm quantities, over a wide range of wavenumber pairs and for a wide range of Reynolds numbers. The modes we study are listed in table 1, where each mode is represented by a unique wavenumber pair (k_x, k_z).

Specifically, the considered modes for each flow case are as follows.

(i) The dominant low Reynolds (DLR) mode – corresponds to the most dominant mode observed in the contour map of $\|\mathscr{H}_{\nabla}\|^{-1}_{\mu_{\Delta_{nr}}}$ at a subcritical Reynolds number for each base flow. These Reynolds numbers are $Re = 358$ for Couette, $Re = 400$ for Blasius and $Re = 690$ for plane Poiseuille base flows. These particular Reynolds numbers were chosen for the cases of Couette and plane Poiseuille flows to equal the Reynolds numbers that were used in Liu & Gayme (2021) and Mushtaq *et al.* (2023), to provide a validation of our results with the results of these works.

(ii) The TS mode – set using the smallest k_z in our numerical domain, which is $k_{z_{min}} = 10^{-2}$. For the case of Couette flow, the k_x value is taken to be $k_x = \arg\max \|\mathscr{H}_{\nabla}\|_{\infty}(k_x, k_{z,min})$, i.e. the streamwise wavenumber argument of the highest value of $\|\mathscr{H}_{\nabla}\|_{\infty}(k_x, k_z)$. For the cases of plane Poiseuille and Blasius base flows, the k_x component of the TS mode associated with the critical mode (according to LST) becomes unstable at the lowest Reynolds number according to LST (Schmid *et al.* 2002). Monitoring this mode is very useful to discuss different aspects of our analysis with respect to LST.

(iii) The spanwise periodic streak (SPS) mode – corresponds to the smallest k_x value in our numerical domain, which is $k_{x,min} = 10^{-4}$, coupled with the k_z values that are observed to be most dominant on the contour maps of $\|\mathscr{H}_{\nabla}\|^{-1}_{\infty}$. The unstructured case is selected following the extensive literature that utilised unstructured-like input–output methodologies where streaks were reported to be dominant (Reddy & Henningson 1993; Schmid & Henningson 1994; Schmid 2000; Bamieh & Dahleh 2001; Jovanovic 2004; Jovanović & Bamieh 2004, 2005).

(iv) The dominant high Reynolds (DHR) mode – observed only for Couette base flow and corresponds to the most dominant mode of $\|\mathscr{H}_{\nabla}\|^{-1}_{\mu_{\Delta_{nr}}}$ at a high Reynolds number, which is selected to be $Re = 8000$.

4.1. *Couette base flow*

In this section we present the results of our analysis for the Couette base flow profile of the form $U = y$. In figure 3 we show the most dominant flow structures in terms

https://doi.org/10.1017/jfm.2026.11214 Published online by Cambridge University Press

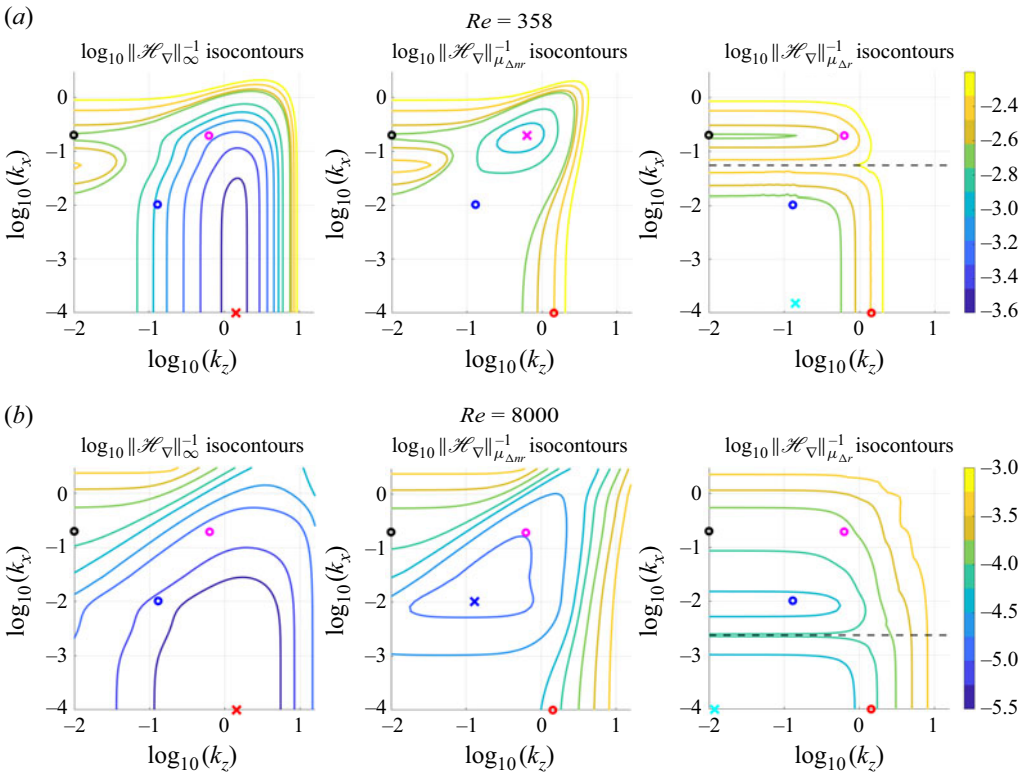


Figure 3. Contour plots in logarithmic scale of (from left to right): $\|\mathscr{H}_\nabla\|_\infty^{-1}$, $\|\mathscr{H}_\nabla\|_{\mu_{\mathbf{\Delta}_{nr}}}^{-1}$ and $\|\mathscr{H}_\nabla\|_{\mu_{\mathbf{\Delta}_r}}^{-1}$ at (*a*) $Re = 358$ and (*b*) $Re = 8000$ for Couette flow. The most dominant mode is marked by an X (cyan colour indicates that the mode's (k_x, k_z) value is not denoted in the table), whereas the other modes from table 1 are marked by coloured circles (magenta – DLR mode, black – TS mode, red – SPS mode, blue – DHR mode). Results are shown for (*a*) $Re = 358$ and (*b*) $Re = 8000$.

of $\|\mathscr{H}_\nabla\|_\infty^{-1}(k_x, k_z)$, $\|\mathscr{H}_\nabla\|_{\mu_{\mathbf{\Delta}_{nr}}}^{-1}(k_x, k_z)$ and $\|\mathscr{H}_\nabla\|_{\mu_{\mathbf{\Delta}_r}}^{-1}(k_x, k_z)$ for both of the Reynolds numbers $Re = 358$ (figure 3*a*) and $Re = 8000$ (figure 3*b*). The Reynolds number $Re = 358$ was chosen to be the same as used in Liu & Gayme (2021) and Mushtaq *et al.* (2024), to validate our results with these works. The value $Re = 8000$ was selected arbitrarily after the post-critical value observed in experiments. We chose a very high value to demonstrate that the stability characteristics do not change drastically when changing the Reynolds number for Couette flow. Over these contour maps, we overlay the modes from table 1. The most dominant mode is marked by an X symbol. If the most dominant mode is not denoted in table 1, it is coloured in cyan. We note that the relationships between the three types of amplification satisfy the relation in (2.29) for both Reynolds numbers, i.e. $\|\mathscr{H}_\nabla\|_{\mu_{\mathbf{\Delta}_r}}(k_x, k_z) \leqslant \|\mathscr{H}_\nabla\|_{\mu_{\mathbf{\Delta}_{nr}}}(k_x, k_z) \leqslant \|\mathscr{H}_\nabla\|_\infty(k_x, k_z)$. Here, $\|\mathscr{H}\|_{\nabla\infty}^{-1}$ reaches values lower than $\|\mathscr{H}_\nabla\|_{\mu_{\mathbf{\Delta}_{nr}}}^{-1}$ and $\|\mathscr{H}_\nabla\|_{\mu_{\mathbf{\Delta}_r}}^{-1}$, respectively, as discussed in § 2.5.

The use of a structured approach for both cases (repeated and non-repeated approaches) leads to an increased stability threshold. The dominant structures that arise in the unstructured case are streamwise elongated structures, whereas oblique modes become the most dominant structures in structured cases, which is more clearly evident in the non-repeated blocks case. The latter result agrees better with DNS and nonlinear optimal perturbation (NLOP)-based predictions than with traditional linear input–output methods (Prigent *et al.*

https://doi.org/10.1017/jfm.2026.11214 Published online by Cambridge University Press

2003; Duguet *et al.* 2010*b*). The contour map of $\|\mathscr{H}_{\nabla}\|^{-1}_{\mu_{\mathbf{\Delta}_{nr}}}$ shows a most dominant oblique wave mode of $(k_x, k_z) \approx (0.1, 1)$, which overpowers the streamwise elongated structures that are also evident on the same colour map by an order of magnitude. It was stated in Liu & Gayme (2021), 'this result is consistent with findings of Reddy *et al.* (1998) showing that oblique waves require less perturbation energy to trigger turbulence in plane Couette flow than streamwise vortices.' As we will show next, the observed dominance of oblique waves is affected by the type of uncertainty that is considered and the Reynolds number. In the case of $\|\mathscr{H}_{\nabla}\|^{-1}_{\mu_{\mathbf{\Delta}_r}}$, where repeated uncertainty is considered, the lowest stability threshold region that is evident in $\|\mathscr{H}_{\nabla}\|^{-1}_{\mu_{\mathbf{\Delta}_r}}$ spreads over a wide range of modes in the bottom left quadrant of the domain, corresponding to a wide range of dominant oblique modes. This result is consistent with the results of Mushtaq *et al.* (2024) for $Re = 358$.

We note that while the relationship in (2.29) shows that $\|\mathscr{H}_{\nabla}\|^{-1}_{\mu_{\mathbf{\Delta}_r}}$ provides a closer bound than $\|\mathscr{H}_{\nabla}\|^{-1}_{\mu_{\mathbf{\Delta}_{nr}}}$ to the accurate value $\|\mathscr{H}_{\nabla}\|^{-1}_{\mu_{\mathbf{\Delta}_\mu}}$ on velocity perturbations from a stability viewpoint, there is no guarantee that it represents more accurately the contour plots in the wavenumber domain. Approximations of the structure of the nonlinear term in the NSE by either non-repeating or repeating blocks still may include additional feedback pathways that are not physically associated with nonlinear flow physics, but to a significantly smaller extent than in the unstructured case. Therefore, considering two structured cases (repeated and non-repeated blocks) is important in our analysis, where common features may be associated with flow physics, whereas the differences require further investigation. One such common feature is the shift of dominant modes to lower k_x values with Reynolds number for unstructured and both structured cases, which means this trend is associated with a linear mechanism. This trend agrees with results obtained from stability analysis of optimal disturbance growth (Butler & Farrell 1992; Schmid *et al.* 2002), where it is shown that for Couette flow, the maximum growth is achieved for $k_x Re \sim \mathrm{C}$, where C is some constant value, which means that for a given non-zero k_z, an increase in the Reynolds number results in a decrease of k_x, which corresponds to oblique and Λ-shaped structures that transform to streaks at higher Reynolds numbers (Hwang & Cossu 2010*b*; Dokoza & Oberlack 2023). Observing $\|\mathscr{H}_{\nabla}\|^{-1}_{\mu_{\mathbf{\Delta}_{nr}}}$ (with non-repeated uncertainty) for both Reynolds numbers, we see that there is a change of the most dominant mode with a Reynolds number increase, where the DLR mode (indicated by a magenta coloured circle) of $(k_x, k_z) = (0.196, 0.628)$ for $Re = 358$ in figure 3(*a*) has a larger stability threshold associated with it than the DHR mode (indicated by blue coloured circle) of $(k_x, k_z) = (0.01, 0.13)$ for $Re = 8000$ in figure 3(*b*). Additionally, in both plots, we added a horizontal dashed black line overlaid on the contour maps of $\|\mathscr{H}_{\nabla}\|_{\mu_{\mathbf{\Delta}_r}}$. This horizontal line represents the border between two regions of relatively unstable modes in the contour maps of $\|\mathscr{H}_{\nabla}\|^{-1}_{\mu_{\mathbf{\Delta}_r}}$ for both Reynolds numbers, $Re = 358$ and $Re = 8000$, respectively. This line migrates towards a lower k_x value with the Reynolds number increase, due to the shift of dominant modes to lower k_x values. Thus, it is evident that there is a set of oblique modes with this streamwise wavenumber (of the dashed line) and spanwise wavenumber values of $k_z < 1$ that will exhibit increased stability compared with neighbouring modes.

In the results for the higher Reynolds number, lower stability threshold values are observed for all of the quantities $\|\mathscr{H}_{\nabla}\|^{-1}_{\mu_{\mathbf{\Delta}_r}}(k_x, k_z)$, $\|\mathscr{H}_{\nabla}\|^{-1}_{\mu_{\mathbf{\Delta}_{nr}}}(k_x, k_z)$ and $\|\mathscr{H}_{\nabla}\|^{-1}_{\infty}(k_x, k_z)$. In figure 3(*a*) the smallest perturbations that cause instability have a magnitude of $10^{-3.6}$ for the unstructured case. In figure 3(*b*), significantly lower values appear, with the smallest perturbations, which can cause instability, being of magnitude $10^{-5.5}$ for the unstructured case.

https://doi.org/10.1017/jfm.2026.11214 Published online by Cambridge University Press

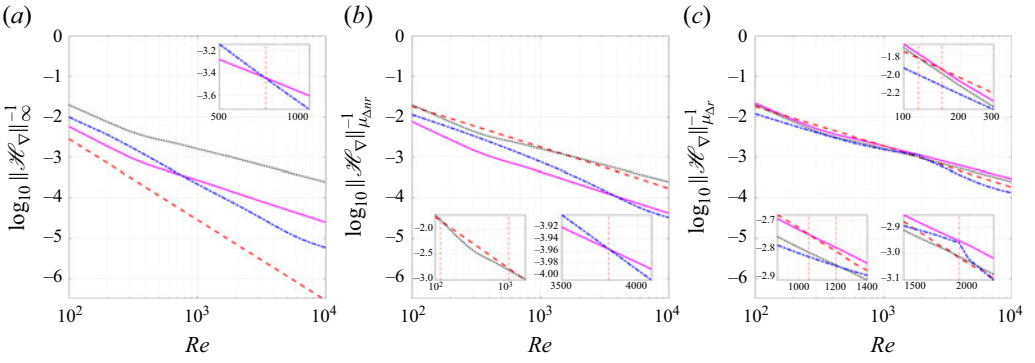


Figure 4. Evolution curves of imposed thresholds due to flow structures associated with preselected modes of interest denoted in table 1 (magenta solid - DLR mode, black dotted - TS mode, red dashed - SPS mode, blue dashed-dotted - DHR mode) for Couette base flow as a function of the Reynolds number in terms of (*a*) $\|\mathscr{H}_\nabla\|_\infty^{-1}$, (*b*) $\|\mathscr{H}_\nabla\|_{\mu_{\Delta nr}}^{-1}$ and (*c*) $\|\mathscr{H}_\nabla\|_{\mu_{\Delta r}}^{-1}$.

Comparing only two Reynolds numbers is insufficient to reveal the interplay between the dominant structures that are evident in these contour maps with Reynolds number variation. Therefore, next, we focus our analysis on key preselected modes of interest from these contour maps and monitor their behaviour for a wide range of Reynolds numbers. In figure 4 we show the evolution of the preselected modes that are listed in table 1 as a function of Reynolds number in the range $Re \in [100, 10\,000]$. The trends from each plot are accompanied by insets of zoomed-in views for certain limited Reynolds number ranges at different locations, revealing the interesting interplay between the mode curves for $\|\mathscr{H}_\nabla\|_{\mu_{\Delta r}}^{-1}$, $\|\mathscr{H}_\nabla\|_{\mu_{\Delta nr}}^{-1}$ and $\|\mathscr{H}_\nabla\|_\infty^{-1}$. In particular, the following insights are gained from these plots.

First, for $\|\mathscr{H}_\nabla\|_\infty^{-1}$ (figure 4*a*), we observe that the SPS mode (red curve) remains the most dominant, i.e. providing the lowest threshold, through the entire range of Reynolds numbers. A higher threshold is shown for the DLR mode (magenta curve) that overpowers the DHR mode (blue curve) for Reynolds numbers up to $Re = 750$, and *vice versa* afterward. The SPS modes are extensively reported in the literature to be the dominant structures for a variety of base flows at different Reynolds numbers when using linear input–output analysis (Bamieh & Dahleh 2001; Jovanovic 2004; Jovanović & Bamieh 2004, 2005; Schmid 2007). Thus, it is not surprising to us that the dominance of the SPS mode for a wide range of Reynolds numbers in the linear analysis represented by $\|\mathscr{H}_\nabla\|_\infty$ is in agreement with previous works. In contrast, this mode is not always dominant if structured analysis is considered. In particular, in the non-repeated case, for $\|\mathscr{H}_\nabla\|_{\mu_{\Delta nr}}^{-1}$ (figure 4*b*), the threshold that is associated to the SPS mode is always higher than the DLR mode (magenta) and the DHR mode (blue) thresholds. The DLR and DHR modes are most dominant for the entire Reynolds number range, where the oblique DLR mode (magenta curve) sets a lower threshold on disturbance to make the flow unstable than the DHR mode (blue curve) for Reynolds number up to $Re \approx 3800$ (denoted by a red vertical dashed line), and *vice versa* afterward. In the repeated case, for $\|\mathscr{H}_\nabla\|_{\mu_{\Delta r}}^{-1}$ (figure 4*c*), we observe first that the oblique DLR mode (magenta curve) provides the highest threshold (out of the four modes that were tested) for the entire range of Reynolds numbers that were considered. Second, the oblique DHR mode (blue curve) is the most dominant mode for $Re < 900$ and $Re > 3500$, whereas in the range $900 < Re < 3500$, the SPS mode (red curve) imposes a slightly lower threshold on perturbation magnitudes for instability to occur than the DHR mode. The blue curve trend is shown to be decreasing, but with a subtle kink at $Re \approx 1900$

https://doi.org/10.1017/jfm.2026.11214 Published online by Cambridge University Press

where the DHR mode drops close to the DLR mode value and then grows again. This kink can be explained by inspecting the contour maps of $\|\mathscr{H}_{\nabla}\|^{-1}_{\mu_{\boldsymbol{\Delta}_r}}$. In figures 3($a$) and 3($b$) we mark dashed horizontal lines representing modes that are stable for larger perturbations, dividing two distinct regions of relative instability for both Reynolds numbers, $Re = 358$ and $Re = 8000$, respectively. This horizontal line is located at $k_x \approx 0.05$ for $Re = 358$, i.e. above the k_x value of the DHR mode (blue circle) – which is defined by the wavenumber pair $(k_x, k_z) = (0.01, 0.13)$ – whereas it shifts towards $k_x \approx 0.0025$, below the k_x value of the DHR mode at $Re = 8000$. This means that when this line migrates towards lower streamwise wavenumbers with a Reynolds number increase, it intersects the $k_x = 0.01$ value at $Re \approx 1900$ where this line matches the same k_x value of the DHR mode.

Second, the TS mode (black curve) imposed threshold is the highest in the unstructured case for all Reynolds numbers, whereas for both $\|\mathscr{H}_{\nabla}\|^{-1}_{\mu_{\boldsymbol{\Delta}_r}}$ (figure 4c) and $\|\mathscr{H}_{\nabla}\|^{-1}_{\mu_{\boldsymbol{\Delta}_{nr}}}$ (figure 4b), the TS mode imposed threshold is higher than the SPS mode threshold (red curve) for almost the entire range of Reynolds numbers that were considered, besides a limited range between $200 < Re < 700$. When using the structured analysis, the most dominant mode changes with the Reynolds number, demonstrating the importance of looking at a range of Reynolds numbers as opposed to a single one to understand the full physical behaviour and stability characteristics of the flow system at hand.

Third, we note that for all Reynolds numbers and modes tested, the curve trends of the most dominant modes agree with the relationship in (2.29) that holds for all Reynolds numbers as expected. In particular, one can observe that the graphs of all of the chosen modes for both of the structured quantities, $\|\mathscr{H}_{\nabla}\|^{-1}_{\mu_{\boldsymbol{\Delta}_{nr}}}$ and $\|\mathscr{H}_{\nabla}\|^{-1}_{\mu_{\boldsymbol{\Delta}_r}}$, remain less spread out than in the case of $\|\mathscr{H}_{\nabla}\|^{-1}_{\infty}$ through the whole range of Reynolds numbers, which is mostly apparent for $\|\mathscr{H}_{\nabla}\|^{-1}_{\mu_{\boldsymbol{\Delta}_r}}$. This observation correlates with the number of constraints imposed on the amplification routes that yield the hierarchical relation of subsets in (2.28). Here, all of the modes impose similar thresholds on the magnitude of perturbations that can be supported by the flow without losing stability. The stability margin represented by $\|\mathscr{H}_{\nabla}\|^{-1}_{\infty}$ is significantly more strict (with the lowest threshold) than in the structured case with repeated block uncertainty, which is represented by $\|\mathscr{H}_{\nabla}\|^{-1}_{\mu_{\boldsymbol{\Delta}_r}}$. For example, at $Re = 1000$, the system represented by $\|\mathscr{H}_{\nabla}\|^{-1}_{\infty}$ can remain stable up to perturbations of a magnitude of $\|\boldsymbol{u}\| \sim O(10^{-4.5})$, whereas for the system represented by $\|\mathscr{H}_{\nabla}\|^{-1}_{\mu_{\boldsymbol{\Delta}_{nr}}}$, the perturbations magnitude increase to a magnitude of $\|\boldsymbol{u}\| \sim O(10^{-3.5})$, and the system represented by $\|\mathscr{H}_{\nabla}\|^{-1}_{\mu_{\boldsymbol{\Delta}_r}}$ can support perturbations up to a magnitude of $\|\boldsymbol{u}\| \sim O(10^{-3})$. We consider here the results of previous works (Reddy *et al.* 1998; Duguet *et al.* 2010*a*, 2013), which used optimisation methods and DNS to predict the minimal perturbation kinetic energy that induces transition to turbulence. These works predict a minimal kinetic energy between $O(10^{-6})$ and $O(10^{-5})$ to cause transition at $Re = 1000$. Kinetic energy is proportional to the square of velocity magnitude; therefore, it corresponds to the disturbance of $O(10^{-3})$ and $O(10^{-2.5})$, where it is clear that the predictions by $\|\mathscr{H}_{\nabla}\|^{-1}_{\infty}$ are overly strict whereas $\|\mathscr{H}_{\nabla}\|^{-1}_{\mu_{\boldsymbol{\Delta}_{nr}}}$ and $\|\mathscr{H}_{\nabla}\|^{-1}_{\mu_{\boldsymbol{\Delta}_r}}$ produce stability thresholds that better agree with DNS results. Since the main cause for the large difference in stability thresholds between the unstructured and structured approaches is associated with the SPS mode, we conclude that the unstructured analysis exaggerates the effect of SPS compared with the real flow physics. A more thorough comparison between the predictions of our stability criterion and the results from numerical simulations and experimental works is provided in § 5.

https://doi.org/10.1017/jfm.2026.11214 Published online by Cambridge University Press

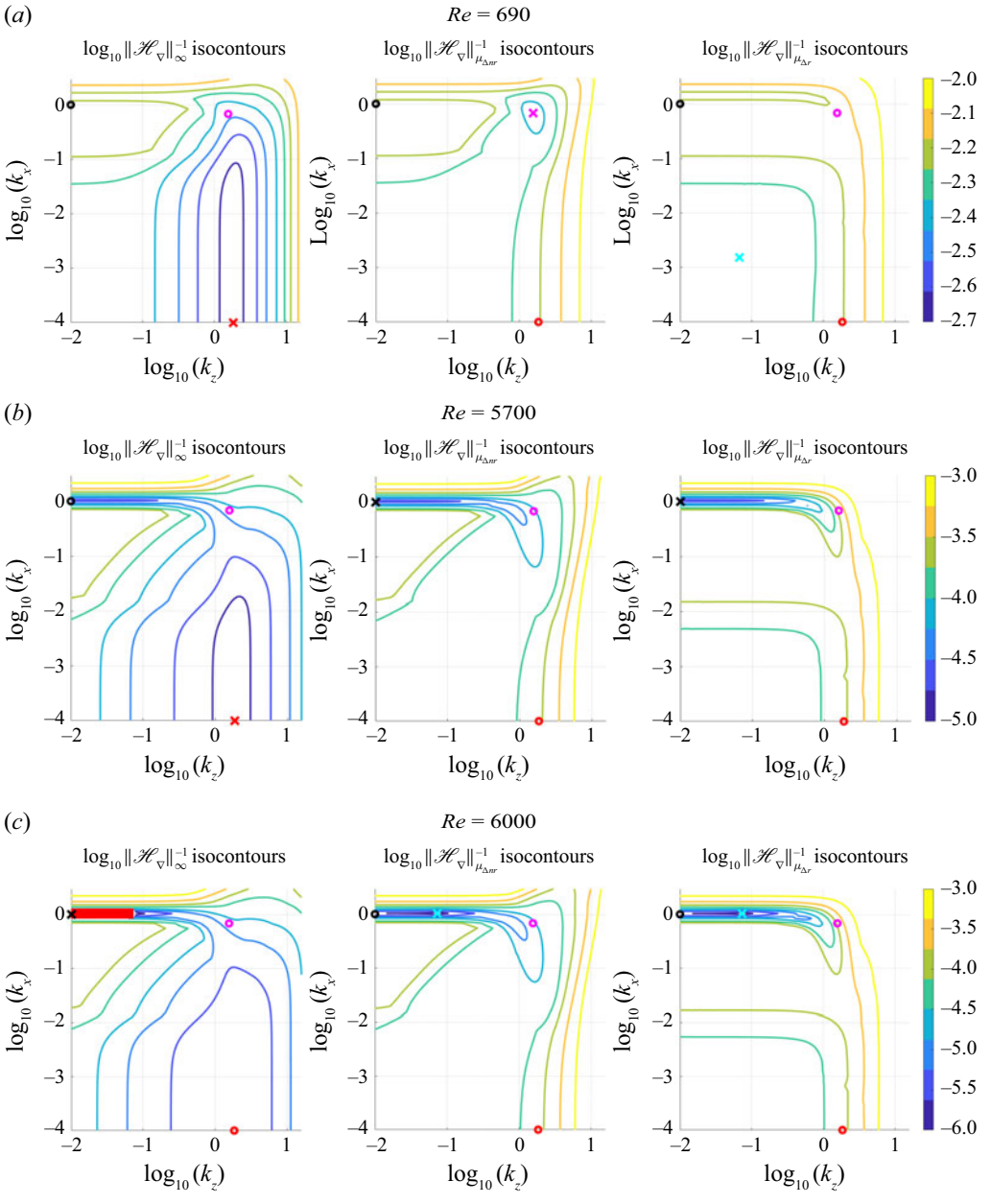


Figure 5. Contour plots in logarithmic scale of (from left to right): $\|\mathscr{H}_\nabla\|_\infty^{-1}$, $\|\mathscr{H}_\nabla\|_{\mu_{\Delta nr}}^{-1}$ and $\|\mathscr{H}_\nabla\|_{\mu_{\Delta r}}^{-1}$ at (*a*) $Re = 690$, (*b*) $Re = 5700$ and (*c*) $Re = 6000$ for plane Poiseuille flow. The most dominant mode is marked by an X (cyan colour indicates that the mode's (k_x, k_z) value is not denoted in the table), whereas the other modes from table 1 are marked by coloured circles (magenta - DLR mode, black - TS mode, red - SPS mode). Results are shown for (*a*) $Re = 690$, (*b*) $Re = 5700$, (*c*) $Re = 6000$.

4.2. *Plane Poiseuille base flow*

In this section we present stability analysis results obtained using the plane Poiseuille base flow profile of the form $U = 1 - y^2$ for three-dimensional perturbations. In figure 5 we show the most dominant flow structures in terms of $\|\mathscr{H}_\nabla\|_\infty^{-1}(k_x, k_z)$, $\|\mathscr{H}_\nabla\|_{\mu_{\Delta nr}}^{-1}(k_x, k_z)$

https://doi.org/10.1017/jfm.2026.11214 Published online by Cambridge University Press

and $\|\mathscr{H}_\nabla\|^{-1}_{\mu_{\mathbf{\Delta}_r}}(k_x, k_z)$ for the Reynolds numbers $Re = 690$ (figure 5*a*), $Re = 5700$ (figure 5*b*) and $Re = 6000$ (figure 5*c*). The Reynolds number $Re = 690$ is the same as used in Liu & Gayme (2021) and Mushtaq *et al.* (2023) and is chosen to validate our results. The Reynolds numbers $Re = 5700$ and $Re = 6000$ are chosen as one is below and one is above the critical Reynolds number, $Re_c = 5772$, predicted by LST for plane Poiseuille flow. Over these contour maps, we overlay the modes from table 1. The most dominant mode is marked by an X symbol. If the most dominant mode is not denoted in table 1, it is coloured in cyan. For the three Reynolds numbers that were tested, the relationship of the norm-like quantities in (2.29), i.e. $\|\mathscr{H}_\nabla\|_{\mu_{\mathbf{\Delta}_r}}(k_x, k_z) \leqslant \|\mathscr{H}_\nabla\|_{\mu_{\mathbf{\Delta}_{nr}}}(k_x, k_z) \leqslant \|\mathscr{H}_\nabla\|_\infty(k_x, k_z)$, is satisfied as in the Couette case.

The use of structured approaches shows that the lowest threshold is governed by dominance of oblique modes rather than the streamwise elongated streaky structures in the unstructured case, similarly to the Couette base flow. Structured case results were found to better agree with the NLOP-based predictions study of Farano *et al.* (2015), in which it was shown that hairpin vortex structures (associated with oblique modes) can be the outcome of a nonlinear optimal growth process in plane Poiseuille flow, in a similar way as streaky structures can be the result of a linear optimal growth mechanism.

It was stated in Liu & Gayme (2021), 'This result is consistent with findings of Reddy *et al.*, (Reddy *et al.* 1998) showing that oblique waves require slightly less perturbation energy to trigger turbulence in plane Poiseuille flow than streamwise vortices.' Similarly to the case of Couette base flow, herein we show that this conclusion is highly affected by the type of uncertainty that is considered and the Reynolds number. In the case of $\|\mathscr{H}_\nabla\|^{-1}_{\mu_{\mathbf{\Delta}_r}}$ the smallest perturbation magnitudes are associated to a wide range of modes, manifested as a uniform region in the bottom left quadrant of the k_x, k_z plane without any obvious dominant oblique mode. Moreover, observing $\|\mathscr{H}_\nabla\|^{-1}_{\mu_{\mathbf{\Delta}_{nr}}}$ (non-repeated uncertainty) for $Re = 5700$ (figure 5*b*) and $Re = 6000$ (figure 5*c*) reveals that as in the case of Couette base flow, the most dominant mode is highly dependent on the Reynolds number. While in figure 5(*a*) the most dominant mode is the DLR mode (indicated by a magenta coloured circle) of $(k_x, k_z) = (1.561, 0.692)$, in figure 5(*b*) the most dominant mode is the TS mode (indicated by a black-coloured circle) of $(k_x, k_z) = (1.02, 10^{-2})$. In figure 5(*c*), where the Reynolds number is increased further to $Re = 6000$, the most dominant mode in the sense of $\|\mathscr{H}_\nabla\|^{-1}_{\mu_{\mathbf{\Delta}_{nr}}}$ shifts again to be an oblique mode located between the DLR mode and the TS mode on the k_x, k_z domain.

Increasing the Reynolds number from the subcritical value $Re = 690$ to $Re = 5700$ (as shown in figure 5*b*) leads to the dominance of the TS mode and slightly oblique TS modes (represented by a streamwise wavenumber of $k_x \approx 1$ and a spanwise wavenumber of $k_z \ll 1$), which impose a very low threshold for instability to occur for unstructured and both structured cases. Further increasing the Reynolds number to $Re = 6000$ (as shown in figure 5*c*) causes a difference in the stability characteristics between the structured approaches ($\|\mathscr{H}_\nabla\|^{-1}_{\mu_{\mathbf{\Delta}_r}}$ and $\|\mathscr{H}_\nabla\|^{-1}_{\mu_{\mathbf{\Delta}_{nr}}}$) and the unstructured ($\|\mathscr{H}_\nabla\|^{-1}_\infty$) approaches. While in the contour maps of $\|\mathscr{H}_\nabla\|^{-1}_{\mu_{\mathbf{\Delta}_r}}$ and $\|\mathscr{H}_\nabla\|^{-1}_{\mu_{\mathbf{\Delta}_{nr}}}$, TS modes and slightly oblique modes govern the lowest threshold on perturbations up to a magnitude of $O(10^{-6})$, in the contour map of $\|\mathscr{H}_\nabla\|^{-1}_\infty$ the imposed threshold governed by the same modes drops to an infinitesimally small value, i.e. the flow will lose stability for perturbations of any size (even asymptotically small), indicated by the red rectangle in figure 5(*c*), which corresponds to $\|\mathscr{H}_\nabla\|^{-1}_\infty \to 0$.

Next, we study the effect of Reynolds numbers on stability threshold over a wide range in plane Poiseuille flow. In figure 6 we show the evolution of $\|\mathscr{H}_\nabla\|^{-1}_{\mu_{\mathbf{\Delta}_r}}$, $\|\mathscr{H}_\nabla\|^{-1}_{\mu_{\mathbf{\Delta}_{nr}}}$

https://doi.org/10.1017/jfm.2026.11214 Published online by Cambridge University Press

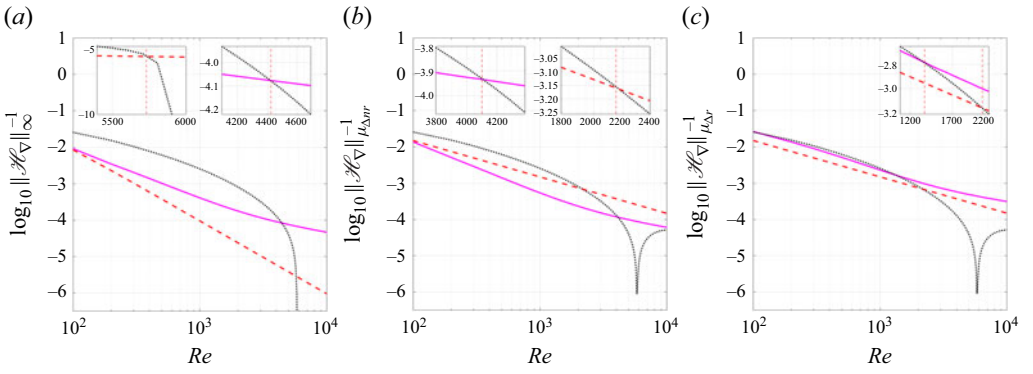


Figure 6. Evolution curves of imposed thresholds due to flow structures associated to preselected modes of interest denoted in table 1 (magenta solid - DLR mode, black dotted - TS mode, red dashed - SPS mode) for plane Poiseuille base flow as a function of the Reynolds number in terms of (*a*) $\|\mathscr{H}_\nabla\|_\infty^{-1}$, (*b*) $\|\mathscr{H}_\nabla\|_{\mu_{\Delta nr}}^{-1}$ and (*c*) $\|\mathscr{H}_\nabla\|_{\mu_{\Delta r}}^{-1}$.

and $\|\mathscr{H}_\nabla\|_\infty^{-1}$ for the chosen modes of interest as a function of the Reynolds number in the interval $Re \in [100, 10000]$. The trends in each graph are accompanied by insets of zoomed-in views for a limited Reynolds number range at different locations, revealing the interesting interplay between the dominance of modes for $\|\mathscr{H}_\nabla\|_{\mu_{\Delta r}}^{-1}$, $\|\mathscr{H}_\nabla\|_{\mu_{\Delta nr}}^{-1}$ and $\|\mathscr{H}_\nabla\|_\infty^{-1}$. In particular, four insights are gained from these plots.

First, for the unstructured case of $\|\mathscr{H}_\nabla\|_\infty^{-1}$, we observe that the SPS mode (red) is the most dominant up until very close to $Re = 5772$, the critical Reynolds number that is predicted by LST (Orszag 1971; Schmid *et al.* 2002). The TS mode (black) becomes most dominant, imposing the lowest threshold at proximity and after the critical Reynolds number. When using both of the structured approaches ($\|\mathscr{H}_\nabla\|_{\mu_{\Delta nr}}^{-1}$ and $\|\mathscr{H}_\nabla\|_{\mu_{\Delta r}}^{-1}$), the TS mode becomes the most dominant mode at a lower Reynolds number compared with the unstructured analysis. In the case of $\|\mathscr{H}_\nabla\|_{\mu_{\Delta nr}}^{-1}$, the TS mode becomes the most dominant after $Re \approx 4100$ (marked by a dashed red line in figure 6*b*) and in the case of $\|\mathscr{H}_\nabla\|_{\mu_{\Delta r}}^{-1}$, it becomes dominant at $Re \approx 2175$ (marked by a dashed red line in figure 6*c*). A recent study by Huang *et al.* (2024) showed that in the case of two-dimensional plane Poiseuille flow, TS waves are the optimal perturbation and can cause a sustained transition to turbulence for $Re \geqslant 2400$, in agreement with the results obtained for the case of repeated blocks. considering structured analysis methods. The non-repeated case ($\|\mathscr{H}_\nabla\|_{\mu_{\Delta nr}}^{-1}$) and repeated case ($\|\mathscr{H}_\nabla\|_{\mu_{\Delta r}}^{-1}$) differ mainly in the stability threshold that are imposed by the DLR mode (magenta), which represents an oblique wave mode. The DLR mode imposes a lower stability threshold in the case of $\|\mathscr{H}_\nabla\|_{\mu_{\Delta nr}}^{-1}$ compared with $\|\mathscr{H}_\nabla\|_{\mu_{\Delta r}}^{-1}$ for the entire range of Reynolds numbers that were tested, similarly to the Couette base flow.

Second, the TS mode curve of $\|\mathscr{H}_\nabla\|_\infty^{-1}$ (figure 6*a*) exhibits an asymptotic behaviour where it approaches zero at $Re = 5772$. The fact that $\|\mathscr{H}_\nabla\|_\infty^{-1}$ approaches zero for the critical mode of actuation and the critical Reynolds number predicted by LST is, of course, not a coincidence. Similarly to figure 12, the results of $\|\mathscr{H}_\nabla\|_\infty^{-1} \to 0$ correspond to the flow being unstable even for asymptotically small perturbations, and thus, results that match the predictions of LST are to be expected. It is important to note that even though close to the critical Reynolds number and beyond, a TS wave sets the lowest threshold for disturbance to trigger transition, it does not necessarily translate to transition being caused by a TS mode. Any mode or combination of modes that surpasses the

https://doi.org/10.1017/jfm.2026.11214 Published online by Cambridge University Press

corresponding stability threshold will destabilise the flow system, which consequently may trigger transition. For example, due to a transient growth scenario or the presence of finite-size disturbances in a noisy flow environment.

Third, in the graphs of $\|\mathscr{H}_{\nabla}\|^{-1}_{\mu_{\mathbf{\Delta}_{nr}}}$ (figure 6*b*) and $\|\mathscr{H}_{\nabla}\|^{-1}_{\mu_{\mathbf{\Delta}_{r}}}$ (figure 6*c*), the TS mode curve reaches a finite value minimum exactly at the critical Reynolds number value that is predicted by LST. After this minimum, the values of both $\|\mathscr{H}_{\nabla}\|^{-1}_{\mu_{\mathbf{\Delta}_{nr}}}$ and $\|\mathscr{H}_{\nabla}\|^{-1}_{\mu_{\mathbf{\Delta}_{r}}}$ increase. This minimum has a finite value in contrast to the behaviour of $\|\mathscr{H}_{\nabla}\|^{-1}_{\infty}$, where the TS mode threshold curve asymptotes towards zero. We explain this observation in more detail in § 5, where we show the associated stability diagrams for both unstructured and structured cases. At higher post-critical Reynolds numbers, the most dominant mode shifts to an oblique mode as the Reynolds number increases. Lastly, the curve trends of the dominant modes that arise in our analysis agree with the relationship in (2.29) for all Reynolds numbers.

4.3. *Blasius base flow*

Here, we analyse the effect of the Reynolds number on the stability and the dominant structures in Blasius flow. The Blasius base flow profile is obtained numerically by solving the Blasius equation $f''' + ff'' = 0$ (Schlichting & Gersten 2016), where f' is the normalised base flow velocity varying with a function of the similarity variable $\eta = y/\delta^*$ and δ^* is a displacement thickness. The boundary conditions used for the solution of the Blasius equation are $f(0) = f'(0) = 0$ and $\lim_{\eta\to\infty} f'(\eta) = 1$. In figure 7 we show the most dominant flow structures in terms of $\|\mathscr{H}_{\nabla}\|^{-1}_{\infty}(k_x, k_z)$, $\|\mathscr{H}_{\nabla}\|^{-1}_{\mu_{\mathbf{\Delta}_{nr}}}(k_x, k_z)$ and $\|\mathscr{H}_{\nabla}\|^{-1}_{\mu_{\mathbf{\Delta}_{r}}}(k_x, k_z)$ for the Reynolds numbers $Re = 400$ (figure 7*a*), $Re = 500$ (figure 7*b*) and $Re = 530$ (figure 7*c*). The Reynolds numbers $Re = 500$ and $Re = 530$ are chosen as one is below and one is above the critical Reynolds number, $Re_c = 520$, predicted by LST for Blasius flow (Schmid *et al.* 2002). The Reynolds number $Re = 400$ was chosen to observe the stability characteristics of the flow at a subcritical Reynolds number, which is further away from the critical value. Over these contour maps, we overlay the modes from table 1. The most dominant mode is marked by an X symbol. If the most dominant mode is not denoted in table 1, it is coloured in cyan. For the three Reynolds numbers that were tested, the relationship between norm-like quantities in (2.29) ($\|\mathscr{H}_{\nabla}\|_{\mu_{\mathbf{\Delta}_{r}}}(k_x, k_z) \leqslant \|\mathscr{H}_{\nabla}\|_{\mu_{\mathbf{\Delta}_{nr}}}(k_x, k_z) \leqslant \|\mathscr{H}_{\nabla}\|_{\infty}(k_x, k_z)$) is satisfied, similarly to the cases of Couette flow and plane Poiseuille flow. This in turn shows that the relation in (2.29) is invariant to the base flow geometry considered (at least for the cases we tested).

The most dominant mode of actuation is highly dependent on the Reynolds number and the type of structured uncertainty considered (repeated versus non-repeated). In the case of $\|\mathscr{H}_{\nabla}\|^{-1}_{\mu_{\mathbf{\Delta}_{nr}}}$, the most dominant mode at $Re = 400$ (figure 7*a*) is the DLR mode, which is an oblique mode. However, increasing the Reynolds number causes the most dominant mode to change, as can be observed in figures 7(*b*) and 7(*c*). When using repeated uncertainty ($\|\mathscr{H}_{\nabla}\|^{-1}_{\mu_{\mathbf{\Delta}_{r}}}$), the DLR mode and neighbouring modes have significantly lower stability thresholds.

For Reynolds numbers below Re_c, the quantities $\|\mathscr{H}_{\nabla}\|^{-1}_{\mu_{\mathbf{\Delta}_{r}}}$, $\|\mathscr{H}_{\nabla}\|^{-1}_{\mu_{\mathbf{\Delta}_{nr}}}$ and $\|\mathscr{H}_{\nabla}\|^{-1}_{\infty}$ all display similar characteristics of TS modes and slightly oblique TS modes (represented by a streamwise wavenumber of $k_x \approx 0.3$ and a spanwise wavenumber of $k_z \ll 1$) being the most dominant. At $Re = 400$ (displayed in figure 7*a*), there is a band of TS and slightly oblique TS modes with relatively small stability thresholds for both the unstructured and structured approaches. When increasing the Reynolds number to $Re = 500$ (as shown in figure 7*b*), the TS and slightly oblique TS modes become unstable for significantly

https://doi.org/10.1017/jfm.2026.11214 Published online by Cambridge University Press

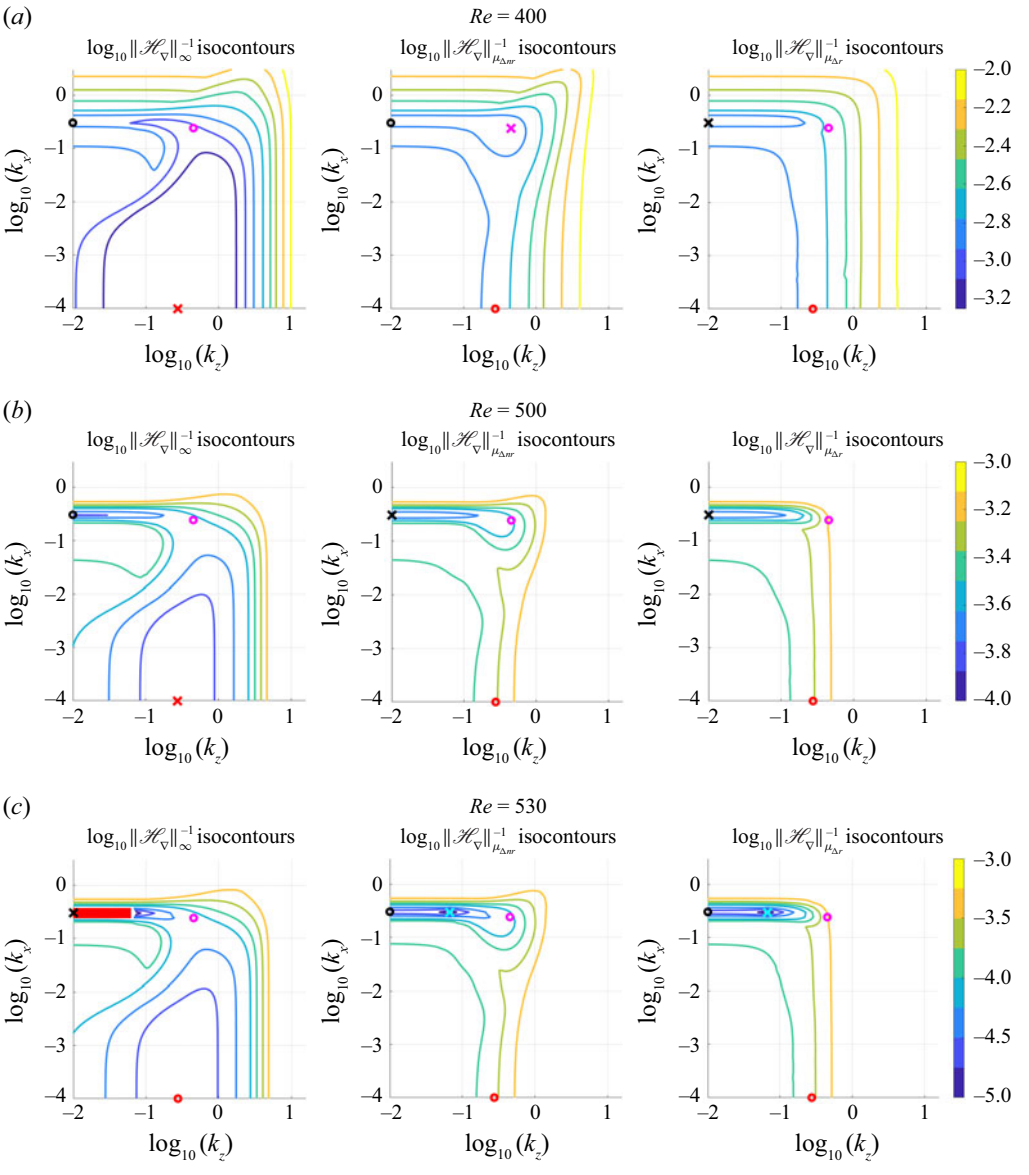


Figure 7. Contour plots in logarithmic scale of (from left to right): $\|\mathscr{H}_\nabla\|_\infty^{-1}$, $\|\mathscr{H}_\nabla\|_{\mu_{\mathbf{\Delta}_{nr}}}^{-1}$ and $\|\mathscr{H}_\nabla\|_{\mu_{\mathbf{\Delta}_r}}^{-1}$ at (*a*) $Re = 400$, (*b*) $Re = 500$ and (*c*) $Re = 530$ for Blasius flow. The most dominant mode is marked by an X (cyan colour indicates that the mode's (k_x, k_z) value is not denoted in the table), whereas the other modes from table 1 are marked by coloured circles (magenta - DLR mode, black - TS mode, red - SPS mode). Results are shown for (*a*) $Re = 400$, (*b*) $Re = 500$, (*c*) $Re = 530$.

smaller perturbations and are the most dominant for both $\|\mathscr{H}_\nabla\|_{\mu_{\mathbf{\Delta}_r}}^{-1}$ and $\|\mathscr{H}_\nabla\|_{\mu_{\mathbf{\Delta}_{nr}}}^{-1}$. In the case of $\|\mathscr{H}_\nabla\|_\infty^{-1}$, these modes have slightly higher stability thresholds than the dominant streamwise elongated streak mode that imposes the lowest threshold. Further increasing the Reynolds number to $Re = 530$ (as shown in figure 7*c*) causes a difference in the stability characteristics of TS and slightly oblique TS modes between the structured approaches ($\|\mathscr{H}_\nabla\|_{\mu_{\mathbf{\Delta}_r}}^{-1}$ and $\|\mathscr{H}_\nabla\|_{\mu_{\mathbf{\Delta}_{nr}}}^{-1}$) and the unstructured ($\|\mathscr{H}_\nabla\|_\infty^{-1}$) approach. In the

https://doi.org/10.1017/jfm.2026.11214 Published online by Cambridge University Press

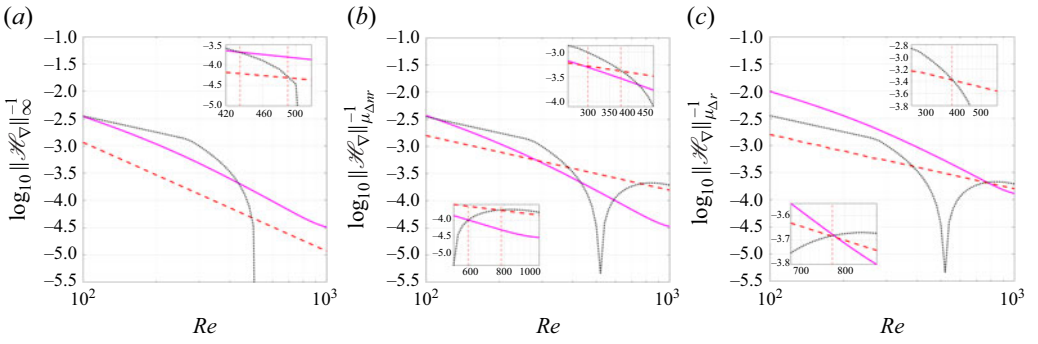


Figure 8. Evolution curves of imposed thresholds due to flow structures associated to preselected modes of interest denoted in table 1 (magenta solid - DLR mode, black dotted - TS mode, red dashed - SPS mode) for Blasius base flow as a function of the Reynolds number in terms of (*a*) $\|\mathscr{H}_\nabla\|_\infty^{-1}$, (*b*) $\|\mathscr{H}_\nabla\|_{\mu_{\Delta nr}}^{-1}$ and (*c*) $\|\mathscr{H}_\nabla\|_{\mu_{\Delta r}}^{-1}$.

contour map of $\|\mathscr{H}_\nabla\|_\infty^{-1}$, the region of slightly oblique TS modes becomes unstable even for asymptotically small perturbations, as in these regions the stability threshold approaches zero (marked as red regions in the contour map). In the structured cases, the most dominant mode of $\|\mathscr{H}_\nabla\|_{\mu_{\Delta r}}^{-1}$ and $\|\mathscr{H}_\nabla\|_{\mu_{\Delta nr}}^{-1}$ shifts to a larger value of k_z, i.e. the mode becomes more oblique, similarly to the case of plane Poiseuille flow.

Next, we explore the stability thresholds variation over a wider range of Reynolds numbers. In figure 8 the evolution of $\|\mathscr{H}_\nabla\|_{\mu_{\Delta r}}^{-1}$, $\|\mathscr{H}_\nabla\|_{\mu_{\Delta nr}}^{-1}$ and $\|\mathscr{H}_\nabla\|_\infty^{-1}$ for the chosen modes of interest as a function of the Reynolds number in the interval $Re \in [100, 1000]$ is shown. The trends in each graph are accompanied by insets of zoomed-in views for a certain Reynolds number range at different locations where intersections between different mode curves are observed for $\|\mathscr{H}_\nabla\|_{\mu_{\Delta r}}^{-1}$, $\|\mathscr{H}_\nabla\|_{\mu_{\Delta nr}}^{-1}$ and $\|\mathscr{H}_\nabla\|_\infty^{-1}$. In particular, these plots reveal the following observations.

First, for the unstructured case of $\|\mathscr{H}_\nabla\|_\infty^{-1}$, we observe that the SPS mode (red) is the most dominant up to $Re = 520$, the critical Reynolds number as predicted by LST (Schmid *et al.* 2002). After this critical Reynolds number, the TS mode (black) becomes the most dominant mode. When using both structured analysis methods ($\|\mathscr{H}_\nabla\|_{\mu_{\Delta nr}}^{-1}$ and $\|\mathscr{H}_\nabla\|_{\mu_{\Delta r}}^{-1}$), the TS mode becomes the most dominant mode at lower-Reynolds-number values as we detail next. In the case of $\|\mathscr{H}_\nabla\|_{\mu_{\Delta nr}}^{-1}$, the TS mode becomes the most dominant mode at $Re \approx 430$ (marked by a dashed red line in figure 8*b*) and in the case of $\|\mathscr{H}_\nabla\|_{\mu_{\Delta r}}^{-1}$, it becomes the most dominant as early as $Re \approx 370$ (marked by a dashed red line in figure 8*c*). The non-repeated case ($\|\mathscr{H}_\nabla\|_{\mu_{\Delta nr}}^{-1}$) and the repeated case ($\|\mathscr{H}_\nabla\|_{\mu_{\Delta r}}^{-1}$) differ only in the magnitude of perturbations that cause instability of the DLR mode (magenta), which represents an oblique wave mode. The perturbation magnitude that causes instability of the DLR mode is slightly smaller for $\|\mathscr{H}_\nabla\|_{\mu_{\Delta nr}}^{-1}$ compared with $\|\mathscr{H}_\nabla\|_{\mu_{\Delta r}}^{-1}$ for all of the tested range of Reynolds numbers, similarly to the cases of Couette and plane Poiseuille flow, and in agreement with (2.29).

Second, in the graph of $\|\mathscr{H}_\nabla\|_\infty^{-1}$ (figure 8*a*) there is an asymptotic behaviour of the TS mode threshold curve that is approaching zero at $Re = 520$. This asymptotic behaviour is explained by LST, which predicts that the chosen TS mode causes the Blasius base flow to become unstable for $Re > 520$ (Schmid *et al.* 2002) for asymptotically small perturbations. In the graphs of $\|\mathscr{H}_\nabla\|_{\mu_{\Delta nr}}^{-1}$ (figure 8*b*) and $\|\mathscr{H}_\nabla\|_{\mu_{\Delta r}}^{-1}$ (figure 8*c*), there is a finite

https://doi.org/10.1017/jfm.2026.11214 Published online by Cambridge University Press

amplitude minimum at the critical Reynolds number predicted by LST, reminiscent of the one observed for the case of plane Poiseuille flow. After this minimum, the value of the TS modes in both $\|\mathscr{H}_\nabla\|^{-1}_{\mu_{\mathbf{\Delta}_{nr}}}$ and $\|\mathscr{H}_\nabla\|^{-1}_{\mu_{\mathbf{\Delta}_r}}$ increase. As in the case of plane Poiseuille, this minimum corresponds to the flow being extremely sensitive to perturbations and very close to the verge of instability. However, this minimum still reaches a finite value in contrast to the behaviour of $\|\mathscr{H}_\nabla\|^{-1}_\infty$ (that approaches zero) due to the imposed structure of the nonlinear term in the Navier–Stokes equation. The existence of this minimum in the graph of the TS mode will be explained similarly to the case of plane Poiseuille flow in more detail in § 5, where we show the associated stability diagrams for both unstructured and structured cases.

Third, using structured analysis creates a much more complicated interplay between the different modes than in the unstructured analysis. In detail, for $\|\mathscr{H}_\nabla\|^{-1}_{\mu_{\mathbf{\Delta}_{nr}}}$ (figure 8*b*), the SPS mode is the most dominant for $Re < 255$ and, for higher Reynolds numbers, the most dominant mode is the DLR mode, in the range $255 < Re < 430$. The TS mode is most dominant for $430 < Re < 590$ and, for higher Reynolds numbers, the DLR mode is again the most dominant. For $\|\mathscr{H}_\nabla\|^{-1}_{\mu_{\mathbf{\Delta}_r}}$ (figure 8*c*), the SPS mode is the most dominant for $Re < 367$. The TS mode is most dominant for $367 < Re < 770$ and, for higher Reynolds numbers, the DLR mode becomes the most dominant. The results for the repeated blocks analysis in figure 8(*c*) show that after $Re = 800$ the oblique DLR mode dominates the flow, setting a threshold value, which is the lowest but very close to the SPS mode curve for both structured cases. Support for such results may be found in the experimental study by Elofsson & Alfredsson (2000), where it was noted that for the post-critical transition process in the Blasius boundary layer, the combined effect of non-modal growth of streaks and a second stage with exponential growth of oblique waves is responsible for the initiation of the final breakdown stage. The intricate relationship between the different modes that set the stability threshold, as depicted in figure 8, highlights the necessity of analysing a broad range of Reynolds numbers. Limiting the examination to a single Reynolds number would result in overlooking significant physical characteristics of the flow system in this case.

Lastly, we note that for all Reynolds numbers, the curve trends of the imposed thresholds that are set by the most dominant modes agree with the relationship we derived in (2.29). As explained in § 2.5, $\|\mathscr{H}_\nabla\|^{-1}_{\mu_{\mathbf{\Delta}_r}}$ is the best approximation available to us for $\|\mathscr{H}_\nabla\|^{-1}_{\mu_{\mathbf{\Delta}_u}}$, which incorporates the accurate structure of the nonlinear term in the NSE. Thus, we expect $\|\mathscr{H}_\nabla\|^{-1}_{\mu_{\mathbf{\Delta}_r}}$ to be the bound on velocity perturbations, which is the closest to the accurate value $\|\mathscr{H}_\nabla\|^{-1}_{\mu_{\mathbf{\Delta}_u}}$ from a stability viewpoint. As denoted in previous sections, there is no guarantee that it represents more accurately the contour plots in the wavenumber domain compared with the $\|\mathscr{H}_\nabla\|^{-1}_{\mu_{\mathbf{\Delta}_{nr}}}$ case. Using the formulation of stability with the small gain theorem shows that instability can occur in Blasius flow at any Reynolds number. Specifically, instability can occur at smaller Reynolds numbers than the critical value predicted via LST, $Re = 520$, given that perturbations of finite magnitude are present in the flow, surpassing the threshold provided by our stability criterion.

The results presented here can be used to explain experimental evidence of subcritical transition in flat plate boundary layers. In the work of Asai & Nishioka (1995), subcritical transition is triggered by energetic hairpin eddies. The boundary layer is found to be stable below $Re_x = 2.8 \times 10^4$, which is equivalent to $Re = 288$ (based on the displacement thickness) for a perturbation magnitude of 0.3 % (as shown in Asai & Nishioka 1995 (figure 3) at $x \approx 100$ mm that correspond to this Reynolds number) at the leading edge (for the case of weak forcing). This magnitude corresponds to a value of $10^{-2.5}$, which is in

https://doi.org/10.1017/jfm.2026.11214 Published online by Cambridge University Press

relatively good agreement with our analysis for the structured two cases, where the imposed threshold by the most dominant mode is $O(10^{-3})$, which is the SPS mode at this Reynolds number. Subcritical transition induced by finite-size perturbations is also observed in DNS studies, such as Cherubini *et al.* (2011) and Vavaliaris, Beneitez & Henningson (2020), where it was found that a finite threshold value exists for $Re = 300$ and $Re = 275$, respectively. In particular, the energy threshold for transition was computed in Vavaliaris *et al.* (2020), where a value of $E_c = 3.64 \times 10^{-2}$ was obtained. This value refers to the combined energy of the velocity perturbation field inside the entire spatial domain, whereas in the current work, we focus only on the specific perturbation of the largest magnitude. For that reason, a comparison between the results can be performed by dividing the energy by the volume of the computational domain reported in Vavaliaris *et al.* (2020) to obtain an energy density value of 1.2×10^{-8}. The square root of this value corresponds to the average magnitude of localised perturbations in the flow, which turns out to be 1.1×10^{-4}. While the value of the largest perturbation magnitude is not provided in their work, it is reasonable to assume that it is significantly larger than the average value computed here. Thus, a maximal perturbation magnitude of $O(10^{-3})$, which was found to be the stability threshold using our methodology, seems reasonable.

5. Critical Reynolds number prediction and comparison with literature

This section focuses on comparing our stability criteria with LST and on validating our analysis of the predicted critical Reynolds number using results from reported experimental and DNS studies. The following two types of analyses are conducted for Couette, plane Poiseuille and Blasius flows.

(i) We draw a direct comparison between our stability analysis approach and predictions of LST, including the reproduction of stability diagrams.
(ii) We determine the critical Reynolds number using our stability criterion and the critical perturbation energy required for transition, and compare them with experimental and DNS results from available literature.

To draw a direct comparison between our stability analysis approach and predictions of LST, we consider here only two-dimensional modes with $k_z = 0$ for two reasons: (i) these modes were shown to be dominant close to critical Reynolds numbers in § 2.3, (ii) to compare our stability diagram with LST results, which are usually obtained for two-dimensional modes, which, according to LST, yield the lowest critical Reynolds number (Schmid *et al.* 2002). In addition, only the non-repeated block case is considered for the structured analysis, since we found no significant difference for $k_z = 0$ compared with the repeated blocks case (see Appendix B), where the non-repeated method is more numerically efficient to compute. For each flow case, we also validate our analysis for a wide range of Reynolds numbers with results from literature, by computation of the critical perturbation energy that causes instability, defined as $E_c = A_c^2/2$, where A_c is the perturbation magnitude (herein we use common notation from the literature).

5.1. *Couette base flow*

In figure 9 we show an example of the stability diagram in the $Re - k_x$ domain, showing only a single isocontour for a threshold value equal to $10^{-2.43} = 3.7 \times 10^{-3}$ for $\|\mathscr{H}_\nabla\|_\infty^{-1}$ at $k_z = 0$. The (Re, k_x) plane is divided into two regions: the stable region is found to the left of the isocontour given the presence of perturbations of magnitude below 3.7×10^{-3}, while the unstable region is found to its right, i.e. at higher Reynolds numbers. In our case,

https://doi.org/10.1017/jfm.2026.11214 Published online by Cambridge University Press

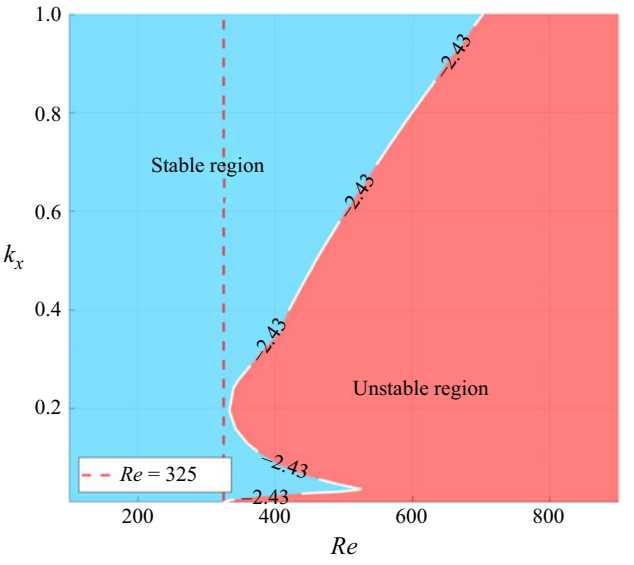


Figure 9. Contour plot of $\|\mathscr{H}_{\boldsymbol{\nabla}}\|_{\infty}^{-1} = 10^{-2.43}$ and stability interpretation based on (2.20) at $k_z = 0$.

the critical Reynolds number for this perturbation magnitude is defined as the smallest Reynolds number for which the perpendicular line (denoted by the red dashed line in the figure) is tangent to the contour of the threshold $\|\mathscr{H}_{\boldsymbol{\nabla}}\|_{\infty}^{-1} = 3.7 \times 10^{-3}$. In this case, the critical Reynolds number turns out to be $Re_c = 325$ for perturbations that are 0.37 % of the characteristic base flow velocity (in the Couette case, it is half the velocity difference between the walls). This critical Reynolds number matches the experimental results of Dauchot & Daviaud (1995) and simulations by Kreiss, Lundbladh & Henningson (1994). In Dauchot & Daviaud (1995), it was noted that very large perturbations are introduced via transverse jet flow injected into the laminar flow, where the information on the exact magnitude was not available. In Kreiss *et al.* (1994), the relation $A_c \sim Re^{-1}$ is established for the critical perturbation amplitude in Couette flow. Considering the Reynolds number $Re = 325$, this relation yields a critical value of $Re^{-1} = 3.1 \times 10^{-3}$ (upper bound on the disturbance by their analysis), which is similar to the value we predict using $\|\mathscr{H}_{\boldsymbol{\nabla}}\|_{\infty}^{-1}$ and also for the structured case, which yields the same results as shown in figure 10. We note that in Kreiss *et al.* (1994) there is a large prefactor of $\sqrt{2000}$ that multiplies Re^{-1}. As noted by Kreiss *et al.* (1994), they compute an upper bound for the perturbation magnitude and not necessarily the exact value. In Kreiss *et al.* (1994), only one initial condition is considered (two counter-rotating vortices added to Stokes' noise), and thus, their result can be significantly higher than the bound for the least stable initial condition. This highlights a significant advantage of our analysis, as we do not require exhaustive simulations of many different initial conditions to obtain the optimal bound on the perturbation magnitude.

The analysis presented here can be extended to any range of threshold values, as shown in figure 10, where we show stability diagrams in the $Re - k_x$ domain at $k_z = 0$, showing several isocontours for different threshold values for both cases: $\|\mathscr{H}_{\boldsymbol{\nabla}}\|_{\infty}^{-1}$ and $\|\mathscr{H}_{\boldsymbol{\nabla}}\|_{\mu_{\boldsymbol{\Delta}_{nr}}}^{-1}$. The stability diagrams in both structured and unstructured cases display very similar behaviour, showing that the structure of the interconnected nonlinearity does not affect the stability characteristics of Couette flow for $k_z = 0$, i.e. if only two-dimensional TS modes are considered. Both subfigures (panels *a* and *b*) show that as the Reynolds number

https://doi.org/10.1017/jfm.2026.11214 Published online by Cambridge University Press

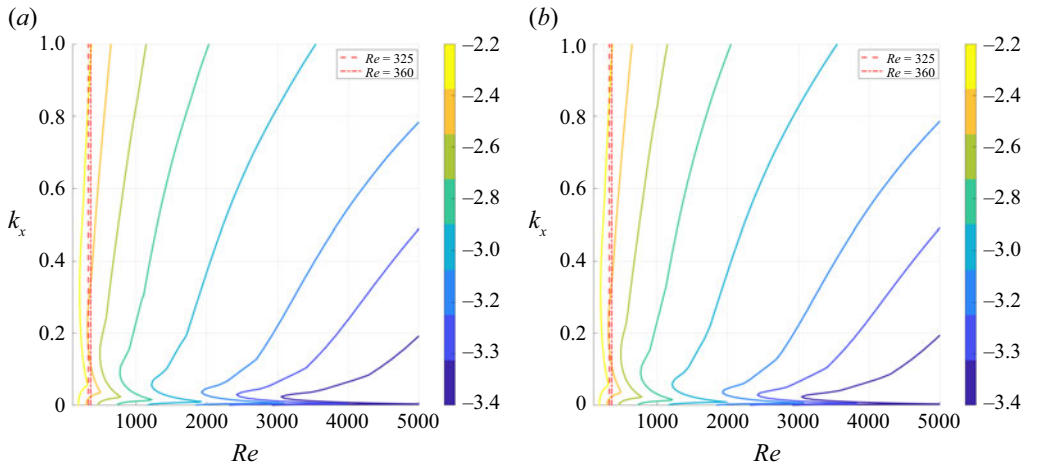


Figure 10. Stability diagrams for Couette flow showing contour plots on the $Re - k_x$ domain for $k_z = 0$ of imposed thresholds of (*a*) $\|\mathscr{H}_\nabla\|_\infty^{-1}$ and (*b*) $\|\mathscr{H}_\nabla\|_{\mu_{\mathbf{\Delta}_{nr}}}^{-1}$.

increases, the flow becomes more sensitive to smaller velocity perturbations. We observe that Couette flow is more sensitive to perturbations characterised by smaller k_x values, especially at higher Reynolds numbers.

Stability analysis via our small gain theorem approach implies that there exists a perturbation of a finite value that could cause the flow to become unstable. With the increase in Reynolds number, the magnitude of perturbation that will not trigger transitioning to turbulence becomes smaller, and thus, there is a higher probability for transition to occur. In contrast to LST, which predicts that Couette flow is asymptotically stable for any Reynolds number (Schmid 2007), our small gain theorem approach provides mathematical proof that Couette flow can become unstable for a finite disturbance magnitude that exceeds a particular bound such as $\|\mathscr{H}_\nabla\|_\infty^{-1}$, $\|\mathscr{H}_\nabla\|_{\mu_{\mathbf{\Delta}_{nr}}}^{-1}$ or $\|\mathscr{H}_\nabla\|_{\mu_{\mathbf{\Delta}_r}}^{-1}$ for any Reynolds number, which agrees with experimental observations, such as Tillmark & Alfredsson (1992), Dauchot & Daviaud (1995), and simulation results (Barkley & Tuckerman 2005; Dou & Khoo 2012) showing transition at $Re = 320 - 370$. In particular, the vertical dashed red lines in figures 10(*a*) and 10(*b*) correspond to $Re = 325$, the critical Reynolds number found experimentally by Dauchot & Daviaud (1995), and the vertical dashed–dotted red lines correspond to $Re = 360$, the critical Reynolds number found experimentally by Tillmark & Alfredsson (1992). In their study, the authors introduced controlled finite-size disturbances of short duration that were made by a solenoid activated, 1 mm diameter fluid jet. However, no information is available on the magnitude of the disturbance. According to our stability criterion, the stability bound depends on the geometric shape of the disturbance (represented by its wavenumber pair k_x, k_z), its temporal frequency ω and its magnitude. Thus, differences in the magnitude of the introduced disturbances, in geometric shape and in the time period between disturbances can all cause the discrepancy between the critical Reynolds number predictions of Tillmark & Alfredsson (1992) and Dauchot & Daviaud (1995).

Next, to validate our analysis for a wide range of Reynolds numbers with results from the literature, we compute the critical perturbation energy that causes instability. In figure 11(*a*) we conduct a comparison between the critical perturbation energy from our analysis versus DNS data from three studies (Reddy *et al.* 1998; Duguet *et al.* 2010*a*, 2013). Figure 11(*a*) shows that the predictions for the critical Reynolds number and the critical

https://doi.org/10.1017/jfm.2026.11214 Published online by Cambridge University Press

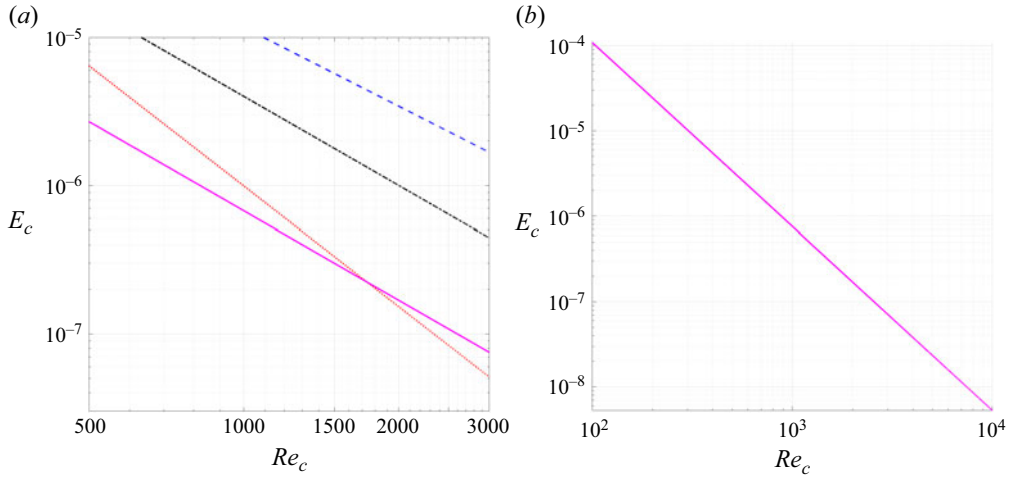


Figure 11. Critical perturbation energy versus critical Reynolds number for Couette flow. (*a*) Our analysis versus results from literature: magenta solid - our results; black dashed-dotted - results from Duguet *et al.* (2010*a*); red dotted - results from Duguet *et al.* (2013), blue dashed - results from Reddy *et al.* (1998). (*b*) Our analysis for a wider range of Reynolds numbers, $Re \in [100, 10000]$.

energy for instability are similar to the prediction made by Duguet *et al.* (2013). While both Reddy *et al.* (1998) and Duguet *et al.* (2010*a*) consider a specific oblique wave scenario, by employing a nonlinear optimisation method, in Duguet *et al.* (2013) a more general transition scenario was considered, leading to lower critical energy predictions. The linear trend (in logarithmic scale) in figure 11(*a*) corresponds to a relationship of the form $E_c \propto Re^{-\gamma}$. Using our methodology, a value of $\gamma \approx 2$ is predicted, similar to the results of Reddy *et al.* (1998) and Duguet *et al.* (2010*a*). However, a value of $\gamma \approx 2.7$ was reported by Duguet *et al.* (2013), which better agrees with our results. It is possible that considering modes with a non-zero spanwise wavenumber can lead to even better agreement. Lastly, in figure 11(*b*) we show that the obtained relationship $E_c \propto Re^{-2}$ is sustained for a wide range of Reynolds numbers, by increasing the domain to $Re \in [100, 10000]$. We note that we only display the results using $\|\mathscr{H}_\nabla\|_\infty^{-1}$, as both the unstructured and structured methods yielded the same results, similarly to the results in figure 10.

5.2. *Plane Poiseuille base flow*

In figure 12 we show stability diagrams for plane Poiseuille flow in the $Re - k_x$ domain at $k_z = 0$, showing several isocontours for different threshold values for both cases: $\|\mathscr{H}_\nabla\|_\infty^{-1}$ (figure 12*a*) and $\|\mathscr{H}_\nabla\|_{\mu_{\Delta_{nr}}}^{-1}$ (figure 12*b*). The dashed red contour in figures 12(*a*) and 12(*b*) corresponds to the neutral curve for Poiseuille base flow computed using eigenvalue analysis (LST), which is shown for comparison with our results.

In figure 12(*a*), as the Reynolds number increases, the threshold on disturbance that is required to make the flow unstable decreases similarly to the case of Couette flow. However, in the case of plane Poiseuille flow, as the threshold decreases, the resulting contours approach the neutral curve obtained by LST. When $\|\mathscr{H}_\nabla\|_\infty^{-1}(k_x, k_z) \to 0$, infinitesimal velocity perturbations will cause the system to become unstable. This is how our small gain formulation of stability relates to LST, according to which, the region within the neutral curve is where the modes are infinitely amplified. The predictions of LST, including critical Reynolds numbers, are valid only for the case of asymptotically small perturbations. Herein, the small gain theorem formulation provides an extension of LST

https://doi.org/10.1017/jfm.2026.11214 Published online by Cambridge University Press

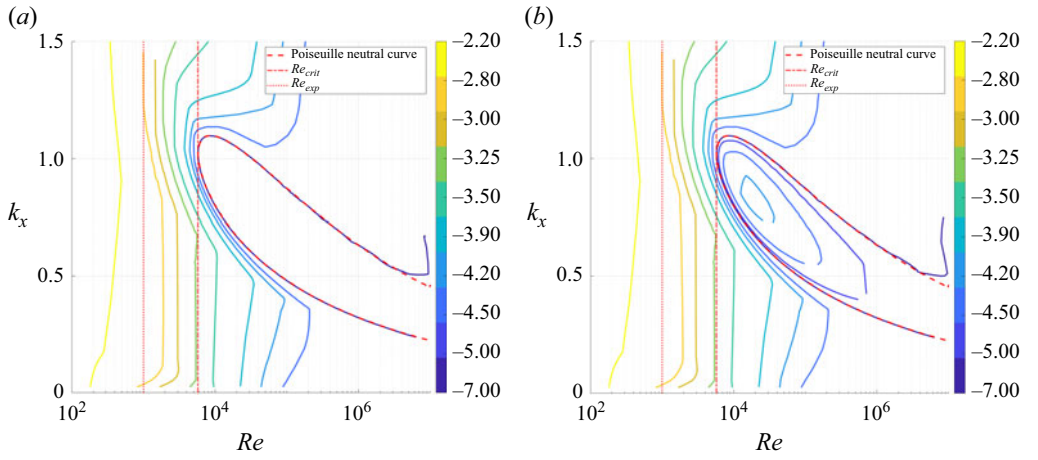


Figure 12. Stability diagrams for plane Poiseuille flow showing contour plots on the $Re - k_x$ domain for $k_z = 0$ of imposed thresholds of (*a*) $\|\mathscr{H}_\nabla\|_\infty^{-1}$ and (*b*) $\|\mathscr{H}_\nabla\|_{\mu_{\mathbf{\Delta}_{nr}}}^{-1}$. The vertical dotted line corresponds to $Re = 1000$ and the dashed-dotted line corresponds to $Re = 5772$. The red dashed contour is the neutral stability contour computed using LST.

and allows us to determine stability based on the magnitude of the perturbations in the flow for any Reynolds number. Using our small gain theorem approach to study transition states shows that instability can occur in plane Poiseuille flow at lower Reynolds numbers than the critical value $Re = 5772$ (denoted by vertical dashed–dotted red lines in the figures) that is predicted via LST and our use of the bounds $\|\mathscr{H}_\nabla\|_\infty^{-1}$ and $\|\mathscr{H}_\nabla\|_{\mu_{\mathbf{\Delta}_{nr}}}^{-1}$. The exact Reynolds number associated with the loss of stability depends on the magnitude of velocity perturbations that exist in the flow field. The flow will become unstable at earlier Reynolds number if the velocity perturbation exceeds the bound of $\|\mathscr{H}_\nabla\|_{\mu_{\mathbf{\Delta}_u}}^{-1}$, which can be approximated by $\|\mathscr{H}_\nabla\|_\infty^{-1}$, $\|\mathscr{H}_\nabla\|_{\mu_{\mathbf{\Delta}_{nr}}}^{-1}$ or $\|\mathscr{H}_\nabla\|_{\mu_{\mathbf{\Delta}_r}}^{-1}$. Thus, experimental observations of subcritical transition in plane Poiseuille flow, such as in Nishioka & Asai (1985) and Sano & Tamai (2016), can be explained by our novel stability criterion. The perturbation magnitude that corresponds to a critical Reynolds number of $Re = 1000$ (denoted by the vertical dotted red lines in the figures) is approximately $10^{-2.9} = 1.1 \times 10^{-3}$ (for both structured and unstructured cases), meaning that perturbations that are 0.11 % of the centreline velocity are needed to be present in the flow for instability to occur for this Reynolds number (Carlson, Widnall & Peeters 1982; Nishioka & Asai 1985). In both studies, finite-size disturbances are introduced to the laminar flow to induce instability, though we could not determine their magnitudes from these studies.

We note that for both unstructured (figure 12*a*) and structured (figure 12*b*) cases, the stability threshold contours plot outside the neutral curve region are very similar, including the obtained infinitesimal thresholds on the curve of the neutral loop itself. The difference between the two is limited to the stability characteristics for threshold values that lie inside the neutral loop. While in figure 12(*a*) any perturbation that corresponds to a mode that is found inside the neutral is deemed unstable. However, in figure 12(*b*) there are contours that are found inside the neutral loop, corresponding to the fact that according to the structured analysis using $\|\mathscr{H}_\nabla\|_{\mu_{\mathbf{\Delta}_{nr}}}^{-1}$ modes that are found inside the neutral loop can be stable given small enough perturbations. The interpretation of contours of the structured quantities $\|\mathscr{H}_\nabla\|_{\mu_{\mathbf{\Delta}_r}}^{-1}$ or $\|\mathscr{H}_\nabla\|_{\mu_{\mathbf{\Delta}_{nr}}}^{-1}$ inside the neutral curve should be treated with caution. The small gain theorem is valid only given that the nominal system $\mathscr{H}_\nabla(k_x, k_z)$ is

https://doi.org/10.1017/jfm.2026.11214 Published online by Cambridge University Press

stable (as we denote in Theorem 1). Linear stability theory predicts an exponentially growing mode within the neutral curve region, driven by linear interactions. Thus, our analysis holds only when the system within the neutral curve region is initially stable. Still, the uncertainty matrices in our analysis may provide a stabilising effect on the interconnected system represented by the loop block diagram in figure 1, allowing the flow to remain stable even at post-critical Reynolds numbers. This is in line with studies by Cossu & Brandt (2002), Fransson *et al.* (2005) that have shown that finite-amplitude streaks stabilise TS instability. Furthermore, nonlinearity in the NSE has also been suggested to provide a stabilising effect, leading to the saturation of linear growth (Schmid *et al.* 2002; McKeon 2017; Jin, Symon & Illingworth 2021). The extent to which these effects are replicated using the current methodology with constant uncertainty matrices, and the implications for stability within the neutral curve, are subject to future study. Results from our analysis can be used to explain the experimental observations of the work by Nishioka *et al.* (1975), in which plane Poiseuille flow is found experimentally to remain stable up to a Reynolds number of $Re = 8000$, which cannot be explained using LST. Our analysis suggests that the perturbation magnitude that leads to the loss of stability at a Reynolds number of $Re = 8000$ is $10^{-4.2}$, which corresponds to a turbulence intensity of 0.006 % of the centreline velocity. This result matches the experimental set-up in Nishioka *et al.* (1975), where the turbulence intensity is reported to be 'essentially less than 0.01 %'.

Next, we validate our analysis for a wide range of Reynolds numbers with results from the literature by computing the critical perturbation energy. Figure 13(*a*) shows that the predictions of the critical Reynolds number and the critical energy for instability are found between the prediction by Parente *et al.* (2022) and the prediction by Reddy *et al.* (1998). While in Reddy *et al.* (1998), a specific oblique wave scenario is considered, Parente *et al.* (2022) employs a nonlinear variational optimisation method to consider a more general transition scenario, leading to lower critical energy predictions. As shown in figure 6, the TS mode is the least dominant for subcritical Reynolds numbers (according to both structured and unstructured methods). Thus, we expect that considering more general cases that include modes with non-zero spanwise wavenumbers will very likely (as discussed in § 4.2) lower the critical perturbation energy predicted by our methodology, making it closer to the results of Parente *et al.* (2022).

The linear trend in figure 13(*a*) corresponds to a relationship of the form $E_c = O(Re^{-\gamma})$. Similarly to the case of Couette flow, a value of $\gamma \approx 2$ is predicted using our methodology. However, this trend does not hold for all Reynolds numbers as we demonstrate in figure 13(*b*), which shows the relationship between the critical energy perturbation and critical Reynolds number for a wider range of Reynolds numbers, $Re \in [100, 15\,000]$. Figure 13(*b*) shows that the linear trend (in logarithmic scale) does not continue for Reynolds numbers above 1700. Instead, there is a rapid decrease of the curve, that asymptotes towards zero at critical Reynolds number $Re = 5772$ for both $\|\mathscr{H}_\nabla\|_\infty^{-1}$ and $\|\mathscr{H}_\nabla\|_{\mu_{\mathbf{\Delta}_{nr}}}^{-1}$ at $Re = 5772$. This result reflects the imposed threshold by the TS mode in figure 6(*b*), where the perturbation energy that is required to cause instability approaches zero, matching the prediction of the critical Reynolds number by LST and our previous discussion on the results of figure 12. The difference between the structured and unstructured cases is restricted to post-critical Reynolds numbers (higher than $Re = 5772$). In detail, $\|\mathscr{H}_\nabla\|_\infty^{-1}$ predicts that any perturbation, even of infinitesimal energy, will cause a transition. However, the structured analysis using $\|\mathscr{H}_\nabla\|_{\mu_{\mathbf{\Delta}_{nr}}}^{-1}$ predicts that while for $Re = 5772$ very small perturbations will cause instability, as the Reynolds number increases beyond this value the critical energy also increases. These results are

https://doi.org/10.1017/jfm.2026.11214 Published online by Cambridge University Press

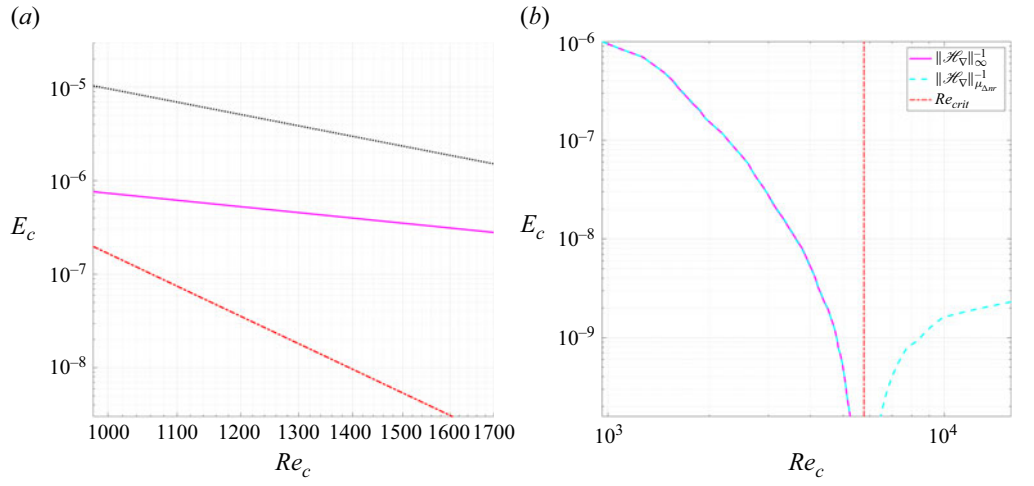


Figure 13. Critical perturbation energy versus critical Reynolds number for plane Poiseuille flow. (*a*) Our analysis versus results from literature: magenta solid - our results; black dotted - Reddy *et al.* (1998); red dashed-dotted - (Parente *et al.* 2022) (minimal energy threshold using large domain). (*b*) Our analysis for the increased range $Re \in [100, 15\,000]$.

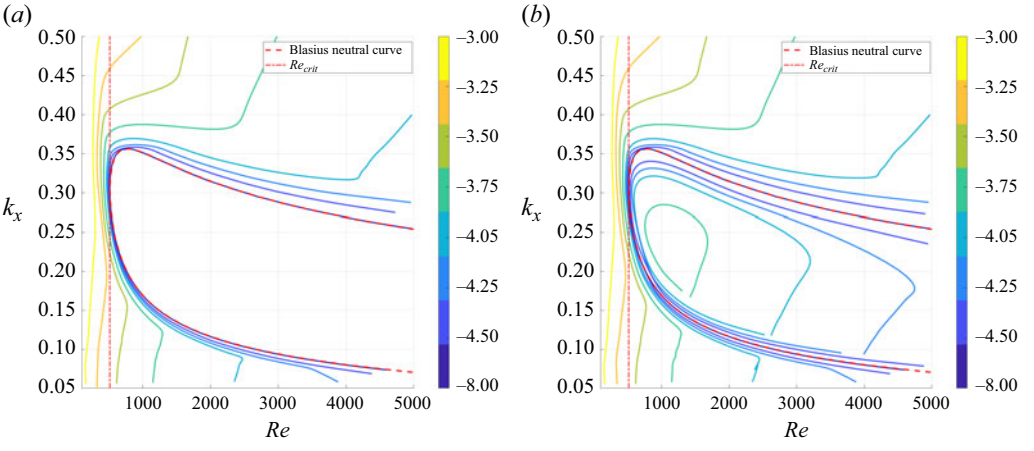


Figure 14. Stability diagrams for Blasius flow showing contour plots on the $Re - k_x$ domain for $k_z = 0$ of imposed thresholds of (*a*) $\|\mathscr{H}_\nabla\|_\infty^{-1}$ and (*b*) $\|\mathscr{H}_\nabla\|_{\mu_{\Delta nr}}^{-1}$. The vertical dashed–dotted line corresponds to $Re = 520$ and the red-dashed contour is the neutral stability contour computed using LST.

consistent with the discussion regarding figure 12(*b*), in which thresholds on perturbation magnitude for stability exist inside the neutral curve.

5.3. *Blasius base flow*

Stability diagrams showing contour plots of threshold on disturbance magnitude using $\|\mathscr{H}_\nabla\|_\infty^{-1}$ and $\|\mathscr{H}_\nabla\|_{\mu_{\Delta nr}}^{-1}$ for Blasius flow are shown in figures 14(*a*) and 14(*b*), respectively. The dashed red curve in both figures corresponds to the so-called 'banana' neutral curve for Blasius base flow, as predicted by LST, and the vertical dashed–dotted red lines correspond to $Re = 520$, the critical Reynolds number predicted by LST for Blasius

https://doi.org/10.1017/jfm.2026.11214 Published online by Cambridge University Press

flow. These plots show that as the Reynolds number increases, the perturbation magnitude that is required to make the flow unstable decreases, similar to the cases of Couette and plane Poiseuille flows. Additionally, as the threshold magnitude decreases, the resulting threshold contours approach the neutral curve obtained via LST, as observed for the case of plane Poiseuille flow. This result shows once again that imposing an infinitesimally small threshold on velocity perturbations leads our analysis to converge to the results of LST, while extending them by allowing us to assess stability in the presence of finite-amplitude perturbations.

Both diagrams for unstructured and structured cases show a very similar topology of threshold isolines outside and on the neutral loop region. Whereas, inside the neutral loop of the structured case diagram (figure 14*b*), there are finite-size threshold contours present. Imposing structure should integrate some aspects of nonlinearity in the computation of $\|\mathscr{H}_{\nabla}\|^{-1}_{\mu_{\mathbf{\Delta}_{nr}}}$, causing the flow to become stable for small finite-sized perturbations inside the neutral loop. This is in contrast to the unstructured case, which predicts any mode inside the neutral loop to be unstable for any perturbation magnitude. However, the presence of a stability threshold isoline inside the neutral curve should be treated with caution, as explained in § 5.2 due to the inherent assumption of the small gain theorem that the interconnected system should be initially stable. It is shown to be feasible to enter the post-critical Reynolds number region, while keeping the flow stable via a nonlinear route to transition as reported in Cherubini *et al.* (2011, 2012), where a finite perturbation magnitude is determined for causing transition of Blasius flow at a Reynolds number of $Re = 610$. This result is in agreement with our results for the structured case, as illustrated in figure 14(*b*). In particular, in Cherubini *et al.* (2012) a critical energy value (of the entire velocity perturbation field) of $E_c = 4.4 \times 10^{-3}$ is obtained for this Reynolds number. As explained in the last paragraph of § 4.3, the average magnitude of perturbations in the flow can be computed given the energy, yielding an average magnitude of $3.3 \times 10^{-4} = 10^{-3.5}$. This value is slightly higher than the value predicted in figure 14(*b*), which is approximately $10^{-4.05}$. This difference can perhaps be attributed to approximating the structure of the nonlinear term in the NSE by non-repeated blocks, as we expect lower stability margin predictions using the exact structure according to (2.29), and also may be due to not accounting for non-parallel effects of the boundary layer in the current study.

Lastly, we now turn our attention to computing the critical energy perturbation for the transition of Blasius flow. Figure 15(*a*) displays the relationship between the critical perturbation energy and the critical Reynolds number on a logarithmic scale, defined similarly as in the cases of Couette and Poiseuille flows. The linear trend in logarithmic scale in figure 15(*a*) corresponds to a relationship of the form $E_c = O(Re^{-\gamma})$. Similarly to the previous cases, a value of $\gamma \approx 2$ is predicted using our methodology. This linear trend holds up to about $Re_c = 320$, after which there is a rapid drop in the critical perturbation energy, as shown in figure 15(*b*) that shows the same relationship between the critical perturbation energy and Reynolds number for a larger range of $Re \in [0, 1100]$. Similar to the observed behaviour for plane Poiseuille flow, the E_c curve asymptotes towards zero at $Re = 520$ for both structured and unstructured cases. The observed trend change in the curve after $Re = 300$ shown in figure 15(*b*) can be explained by a shift in the dominant flow structure that is associated with the least stable mode.

For $Re > 520$, the energy curve for structured methods departs from the unstructured case, exhibiting similar behaviour as the TS mode in figure 8(*b*), which we discussed in detail for the case of plane Poiseuille flow in § 5.2, and will not repeat it here again for brevity.

https://doi.org/10.1017/jfm.2026.11214 Published online by Cambridge University Press

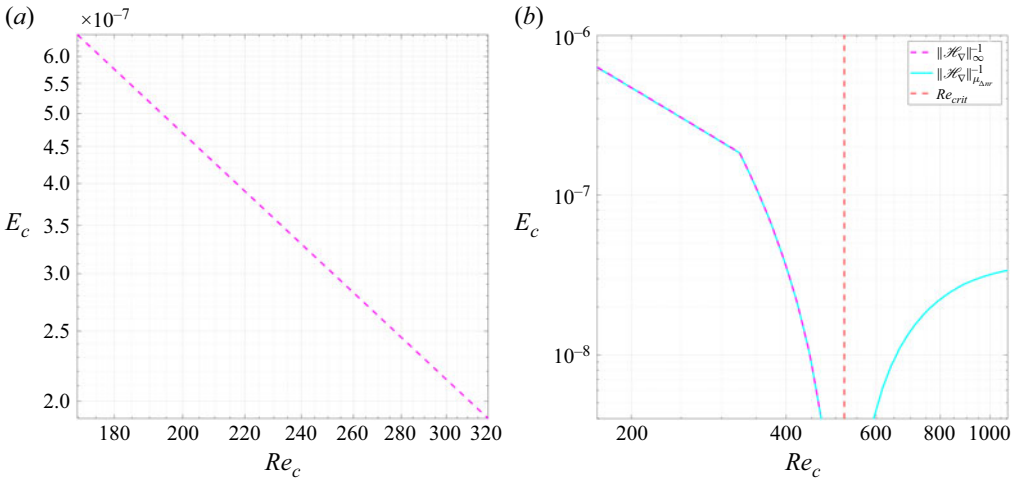


Figure 15. Critical perturbation energy versus critical Reynolds number for Blasius flow via our analysis: (*a*) for a limited range of *Re* up to 320, (*b*) for an increased range of Reynolds numbers up to 1100.

Details on validation of our stability criterion for Blasius flow with some results from experimental studies from literature are provided in the previous § 4.3 (last paragraph), where we discuss the general case for our analysis with non-zero k_z, which is associated with an oblique transition scenario.

6. Conclusions

Herein, we propose a novel stability criterion based on the small gain theorem coupled with unstructured and structured input–output analyses. The criterion provides an upper bound for velocity perturbations that ensures stability. Our stability criterion does not guarantee a transition, but provides an estimate of a threshold for disturbance magnitude that will trigger flow instability. We employ three different input–output approaches for modelling nonlinearity (unstructured, structured with non-repeating blocks and structured with repeating blocks). In particular, we show that the imposed threshold obtained by these three methods complies with a hierarchical relationship based on set inclusion that we obtained in (2.29). According to this hierarchy, the unstructured case is the most conservative, imposing the lowest bound on disturbance magnitude. Moreover, structured input–output with repeating uncertainty analysis provides the closest bound to $\|\mathscr{H}_\nabla\|^{-1}_{\mu_{\mathbf{\Delta}_u}}$, which incorporates the accurate structure of the nonlinear term in the NSE.

This work provides a complementary point of view to non-modal analysis, quantifying the threshold that non-modal growth has to reach to cause flow instability. It allows studying complex transition scenarios that are associated with bypass transition scenarios in the presence of finite-size disturbances and transient growth scenarios caused by a combination of decaying modes. In detail, our framework addresses the discrepancy between the computed critical Reynolds number via LST and the documented Reynolds numbers at which transition is observed in experiments. Stability analysis with our approach is in agreement with previous experimental works, which found that transition can occur at lower Reynolds numbers than the critical Reynolds number predicted by LST, and due to finite amplitude exceeding a certain bound. Non-modal nonlinear stability analysis provides similar thresholds on perturbation magnitude, via computing the evolution of the flow field, iterating over different initial conditions, converging to the one with the

https://doi.org/10.1017/jfm.2026.11214 Published online by Cambridge University Press

smallest magnitude that leads to transition, which is a numerically costly procedure. Our approach is significantly computationally cheaper, allowing us to conduct a more detailed study compared with previous works using non-modal nonlinear approaches, considering a large range of Reynolds numbers and multiple modes in the k_x, k_z domain.

For the limit of infinitesimally small perturbations, we show that our analysis reproduces LST stability diagrams. It is not a coincidence, but it will not always be true. Linear stability theory is based on eigenvalue analysis, which identifies the TS mode as the least stable eigenvalue of the system, and the critical Reynolds number is the Reynolds number at which the growth rate of the TS mode becomes positive. In our analysis, the dominant mode for a given Reynolds number is the mode that sets the lowest threshold on velocity perturbation magnitude to trigger instability. This mode is not necessarily identical to the least stable mode predicted by LST, defined by the largest growth rate. At Reynolds numbers below the critical value, our analysis shows that the TS mode is not the dominant mode, as the threshold is initially set by SPS (in unstructured case) or SPS and later DLR mode in structured cases. However, being the least stable, the TS mode experiences explosive growth, which in turn, makes it the dominant mode that sets the threshold for disturbance magnitude at the proximity of the critical Reynolds number for both plane Poiseuille and Blasius flows, according to structured and unstructured cases.

When approximating nonlinearity using unstructured uncertainty, our results indicate that the region inside the neutral loop is unstable for any perturbation magnitude. In contrast, when using structured uncertainty, our analysis predicts a stable region inside the neutral stability curve predicted by LST, given sufficiently small perturbations for both plane Poiseuille and Blasius flows. The obtained threshold is in agreement with the disturbance level observations in experimental and simulation studies (Nishioka *et al.* 1975; Cherubini *et al.* 2011, 2012) for which the flows remained laminar at post-critical Reynolds numbers in plane channel flow. However, this result should be treated with caution. The small gain theorem guarantees stability only for cases where the nominal system (i.e. the linear interactions represented by $\mathscr{H}_{\mathbf{V}}$) is stable. Linear stability theory predicts that the linear system is unstable inside the neutral loop, due to an exponentially growing mode. Thus, our analysis holds only in the case that the system inside the neutral curve region is initially stable. Nonlinear effects may provide a stabilising effect, explaining our results. The validity of this claim and the accuracy with which our model for nonlinearity represents nonlinear effects in the NSE remain open questions. Furthermore, in spatially evolving, i.e. non-parallel, base flows such as the Blasius boundary layer, the Reynolds number increases as the disturbance propagates downstream. This might cause a disturbance of any size to eventually cross the unstable region, where an infinitesimal threshold around the perimeter of the neutral curve will trigger instability of the flow.

We also use these three input–output approaches to elucidate the interplay between the dominant modes that set the threshold in our stability criterion on disturbance magnitude. We conducted our analysis on three canonical flows – Couette, plane Poiseuille and Blasius for a wide range of Reynolds numbers, which in turn allowed us to obtain new insights on the interplay between flow structures that govern the transition physics of wall-bounded shear flows, which were elusive in past studies. We demonstrate that there is an interplay between flow structures such as streaks, oblique modes and TS waves that govern the flow physics for different Reynolds numbers, where either oblique (Liu & Gayme 2021; Shuai *et al.* 2023) and streak modes (Reddy & Henningson 1993; Schmid & Henningson 1994; Schmid 2000; Bamieh & Dahleh 2001; Jovanovic 2004; Jovanović & Bamieh 2004, 2005) govern the flow at subcritical Reynolds number, setting a finite-size threshold on disturbance magnitude, whereas upon the critical value the TS mode dominates and sets the threshold such that any infinitesimal disturbance would trigger transition at the critical

https://doi.org/10.1017/jfm.2026.11214 Published online by Cambridge University Press

Reynolds value predicted by LST. This is due to the fact, as explained before, that at the proximity of the critical Reynolds number, LST shows that the TS mode becomes unstable close to the critical Reynolds number based on eigenmode analysis, it grows rapidly and overpowers other modes that in turn sets the threshold on disturbance magnitude based on our stability approach.

For a given magnitude of external disturbances, our framework can quantify the threshold below which finite-size disturbances or non-modal growth are allowed to maintain stability. Insights from our stability analysis can lead to improved, efficient control strategies by identifying the forcing that achieves the largest impact on the flow and by predicting flow responses to finite-size actuation forcing. An interesting extension of our study for the future could be to incorporate base flow modifications into our analysis by implementing a structured uncertainty model with a time-varying model for the linearised flow system (Dullerud & Lall 2002).

Declaration of interests. The authors report no conflict of interest.

Appendix A. Derivation of bound on perturbation magnitude

In this appendix we explicitly derive an expression for the norm $\|\boldsymbol{U}_{\Xi}\|_{\infty}$ to show that it is equivalent to the largest perturbation magnitude in the flow, as stated in § 2.4. Here $\boldsymbol{U}_{\Xi}$ is the structured uncertainty applied to the vectorised velocity gradient $\begin{bmatrix}\nabla^T u & \nabla^T v & \nabla^T w\end{bmatrix}^T$ that retains the componentwise structure of the advection term $\boldsymbol{u}\cdot\boldsymbol{\nabla}\boldsymbol{u}$ (Liu & Gayme 2021). The exact expression for $\boldsymbol{U}_{\Xi}$ that captures the nature of the nonlinear term in the NSE after discretisation is

$$\boldsymbol{U}_{\Xi} \equiv \begin{bmatrix} -\boldsymbol{u}_{\xi}{}^T & \boldsymbol{0} & \boldsymbol{0} \\ \boldsymbol{0} & -\boldsymbol{u}_{\xi}{}^T & \boldsymbol{0} \\ \boldsymbol{0} & \boldsymbol{0} & -\boldsymbol{u}_{\xi}{}^T \end{bmatrix}. \tag{A1}$$

Here, $\boldsymbol{u}_{\xi}{}^T \equiv \begin{bmatrix}\mathrm{diag}(u_{\xi}) & \mathrm{diag}(v_{\xi}) & \mathrm{diag}(w_{\xi})\end{bmatrix}$ is a frozen-in-time approximation of the discretised perturbation velocity field. As in (2.25), $u_{\xi}, v_{\xi}, w_{\xi} \in \mathbb{C}^{N_y\times 1}$ represent discretised versions of the perturbations velocity components. To retain concise notation, we denote $\mathrm{diag}(u_{\xi})$ by u_{ξ}^d, and similarly for the other velocity components. Based on (A1), the explicit expression for $\boldsymbol{U}_{\Xi}$ is

$$\boldsymbol{U}_{\Xi} = \begin{bmatrix} -u_{\xi}^d & -v_{\xi}^d & -w_{\xi}^d & 0 & 0 & 0 & 0 & 0 & 0 \\ 0 & 0 & 0 & -u_{\xi}^d & -v_{\xi}^d & -w_{\xi}^d & 0 & 0 & 0 \\ 0 & 0 & 0 & 0 & 0 & 0 & -u_{\xi}^d & -v_{\xi}^d & -w_{\xi}^d \end{bmatrix}. \tag{A2}$$

Using the definition in (A2), we obtain

$$\boldsymbol{U}_{\Xi}^{*} = \begin{bmatrix} -u_{\xi}^{d*} & 0 & 0 \\ -v_{\xi}^{d*} & 0 & 0 \\ -w_{\xi}^{d*} & 0 & 0 \\ 0 & -u_{\xi}^{d*} & 0 \\ 0 & -v_{\xi}^{d*} & 0 \\ 0 & -w_{\xi}^{d*} & 0 \\ 0 & 0 & -u_{\xi}^{d*} \\ 0 & 0 & -v_{\xi}^{d*} \\ 0 & 0 & -w_{\xi}^{d*} \end{bmatrix}. \tag{A3}$$

https://doi.org/10.1017/jfm.2026.11214 Published online by Cambridge University Press

Here, * denotes the conjugate transpose. We multiply the results of (A2) and (A3) to obtain

$$(\boldsymbol{U}_\Xi \boldsymbol{U}_\Xi^*)_{i,j} = \begin{cases} |u_{\xi_i}|^2 + |v_{\xi_i}|^2 + |w_{\xi_i}|^2, & i = j, \\ 0, & \text{else.} \end{cases} \tag{A4}$$

The notation u_{ξ_i} (and similarly for the two other velocity components) denotes the ith entry of u_ξ in the discretised domain, which contains N_y entries.

By the definition of the largest singular value:

$$\bar{\sigma}(\boldsymbol{U}_\Xi) = \sqrt{\bar{\lambda}(\boldsymbol{U}_\Xi \boldsymbol{U}_\Xi^*)}. \tag{A5}$$

Here, $\bar{\lambda}(\cdot)$ represents the largest eigenvalue of a matrix. Since the eigenvalues of a diagonal matrix (such as $\boldsymbol{U}_\Xi \boldsymbol{U}_\Xi^*$) are the diagonal entries, using (A4) and (A5) it is clear that the following is true:

$$\bar{\sigma}(\boldsymbol{U}_\Xi) = \max_i \sqrt{|u_{\xi_i}|^2 + |v_{\xi_i}|^2 + |w_{\xi_i}|^2} \equiv \max_i \|\boldsymbol{u}_{\xi_i}\|_2. \tag{A6}$$

Here, $\boldsymbol{u}_{\xi_i} \equiv \begin{bmatrix} u_{\xi_i} & v_{\xi_i} & w_{\xi_i} \end{bmatrix}^T$. By the definition of the $\mathscr{H}_\infty$ norm (2.10) and using $\boldsymbol{U}_\Xi$ to approximate the continuous matrix operator $\boldsymbol{u}_\Xi$, we obtain the following result:

$$\|\boldsymbol{U}_\Xi\|_\infty = \max_i \|\boldsymbol{u}_{\xi_i}\|_2 \approx \max_{y \in \mathcal{Y}} \|\boldsymbol{u}(y)\|_2. \tag{A7}$$

Here, there is no supremum over temporal frequencies since $\boldsymbol{U}_\Xi$ is constant in the frequency domain; $\mathcal{Y}$ is the relevant domain in the wall-normal direction corresponding to the flow system (for channel flows, $\mathcal{Y} = [-1, 1]$; for boundary layer flows, $\mathcal{Y} = [0, \infty)$); $\max_{y \in \mathcal{Y}} \|\boldsymbol{u}(y)\|_2$ denotes the largest velocity perturbation magnitude that is present in the flow, which we approximate by the maximum velocity perturbation in the discretised domain.

Appendix B. Comparison of structured approaches for $k_z = 0$.

Here, we compare results of $\|\mathscr{H}_\nabla\|_{\mu_{\boldsymbol{\Delta}_{nr}}}$ (non-repeated blocks) and $\|\mathscr{H}_\nabla\|_{\mu_{\boldsymbol{\Delta}_r}}$ (repeated blocks) for TS waves with a spanwise wavenumber of $k_z = 0$. This comparison is made to justify our decision to consider only the non-repeated structured approach in our analysis for two-dimensional modes, presented in § 5. In figure 16 we present colour map plots of $\|\mathscr{H}_\nabla\|^{-1}_{\mu_{\boldsymbol{\Delta}_{nr}}}$, $\|\mathscr{H}_\nabla\|^{-1}_{\mu_{\boldsymbol{\Delta}_r}}$ and the difference $(\|\mathscr{H}_\nabla\|^{-1}_{\mu_{\boldsymbol{\Delta}_r}} - \|\mathscr{H}_\nabla\|^{-1}_{\mu_{\boldsymbol{\Delta}_{nr}}}$ for Blasius base flow and for different k_x and Re values. This computation was made on a low-resolution grid, since it is very numerically demanding to obtain results using the repeated blocks structure. Thus, we consider 29 values of k_x in the domain $k_x \in [0.05, 0.5]$ and 20 Reynolds number values in the domain $Re \in [100, 5000]$.

Figures 16(a) and 16(b) show very similar qualitative behaviours of $\|\mathscr{H}_\nabla\|^{-1}_{\mu_{\boldsymbol{\Delta}_{nr}}}$ and $\|\mathscr{H}_\nabla\|^{-1}_{\mu_{\boldsymbol{\Delta}_r}}$, producing similar thresholds on velocity perturbations across the entire computational domain. The difference in the results between the two structured approaches, which is shown in figure 16(c), is very small across the entire computational domain, with a maximal value of 1.16×10^{-5}. This difference is significantly smaller than the threshold predicted by either method for almost all of the computational domain (apart from very close to the neutral stability curve predicted by LST) and, thus, has no significant effect on any of the results presented in § 5.

https://doi.org/10.1017/jfm.2026.11214 Published online by Cambridge University Press

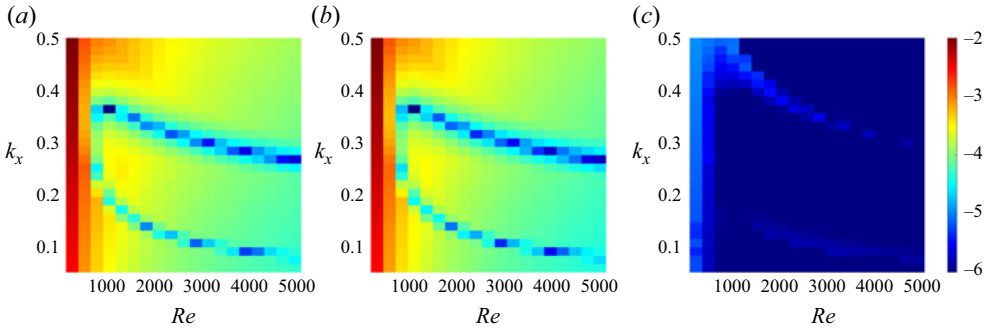


Figure 16. A comparison between the structured analysis methods for Blasius base flow with $k_z = 0$. Colour maps of (*a*) $\|\mathscr{H}_\nabla\|^{-1}_{\mu_{\mathbf{\Delta}_{nr}}}$, (*b*) $\|\mathscr{H}_\nabla\|^{-1}_{\mu_{\mathbf{\Delta}_r}}$, and (*c*) the difference between $\|\mathscr{H}_\nabla\|^{-1}_{\mu_{\mathbf{\Delta}_r}}$ and $\|\mathscr{H}_\nabla\|^{-1}_{\mu_{\mathbf{\Delta}_{nr}}}$. All colour maps are presented on a logarithmic scale.

References

Asai, M. & Nishioka, M. 1995 Boundary-layer transition triggered by hairpin eddies at subcritical Reynolds numbers. *J. Fluid Mech.* **297**, 101–122.

Avila, M., Barkley, D. & Hof, B. 2023 Transition to turbulence in pipe flow. *Annu. Rev. Fluid Mech.* **55** (1), 575–602.

Balas, G., Chiang, R., Packard, A. & Safonov, M. 2005 Robust control toolbox. For Use with Matlab. User's Guide, Version 3.

Bamieh, B. & Dahleh, M. 2001 Energy amplification in channel flows with stochastic excitation. *Phys. Fluids* **13** (11), 3258–3269.

Barkley, D. & Tuckerman, L.S. 2005 Computational study of turbulent laminar patterns in Couette flow. *Phys. Rev. Lett.* **94** (1), 014502.

Bhattacharjee, D., Mushtaq, T., Seiler, P.J. & Hemati, M. 2023 Structured input–output analysis of compressible plane Couette flow. In *AIAA SCITECH 2023 Forum*, *AIAA Paper* 2023-1984.

Burin, M.J. & Czarnocki, C.J. 2012 Subcritical transition and spiral turbulence in circular Couette flow. *J. Fluid Mech.* **709**, 106–122.

Butler, K.M. & Farrell, B.F. 1992 Three-dimensional optimal perturbations in viscous shear flow. *Phys. Fluids* **4** (8), 1637–1650.

Carlson, D.R., Widnall, S.E. & Peeters, M.F. 1982 A flow-visualization study of transition in plane Poiseuille flow. *J. Fluid Mech.* **121**, 487–505.

Chefranov, S.G. & Chefranov, A.G. 2016 Linear instability of plane Couette and Poiseuille flows. *J. Expl Theor. Phys.* **122**, 925–931.

Cherubini, S., De Palma, P., Robinet, J.-C. & Bottaro, A. 2011 The minimal seed of turbulent transition in the boundary layer. *J. Fluid Mech.* **689**, 221–253.

Cherubini, S., De Palma, P., Robinet, J.-C. & Bottaro, A. 2012 A purely nonlinear route to transition approaching the edge of chaos in a boundary layer. *Fluid Dyn. Res.* **44** (3), 031404.

Cohen, J., Philip, J. & Ben-Dov, G. 2009 Aspects of linear and nonlinear instabilities leading to transition in pipe and channel flows. *Phil. Trans. R. Soc. Lond. A* **367** (1888), 509–527.

Cossu, C. & Brandt, L. 2002 Stabilization of Tollmien–Schlichting waves by finite amplitude optimal streaks in the Blasius boundary layer. *Phys. Fluids* **14** (8), L57–L60.

Dauchot, O. & Daviaud, F. 1995 Finite amplitude perturbation and spots growth mechanism in plane Couette flow. *Phys. Fluids* **7** (2), 335–343.

Dokoza, T. & Oberlack, M. 2023 Reynolds number induced growth of the large-scale rolls in plane Couette flow using resolvent analysis. *J. Fluid Mech.* **968**, A23.

Dou, H.-S. & Khoo, B.C. 2012 Direct numerical simulation of turbulent transition for plane Couette flows using full Navier–Stokes equations. In *50th AIAA Aerospace Sciences Meeting Including the New Horizons Forum and Aerospace Exposition*, *AIAA Paper* 2012-891. AIAA.

Duguet, Y., Brandt, L. & Larsson, B.R.J. 2010*a* Towards minimal perturbations in transitional plane Couette flow. *Phys. Rev. E—Stat. Nonlinear Soft Matt. Phys.* **82** (2), 026316.

Duguet, Y., Monokrousos, A., Brandt, L. & Henningson, D.S. 2013 Minimal transition thresholds in plane Couette flow. *Phys. Fluids* **25** (8), 084103.

https://doi.org/10.1017/jfm.2026.11214 Published online by Cambridge University Press

DUGUET, Y., SCHLATTER, P. & HENNINGSON, D.S. 2010*b* Formation of turbulent patterns near the onset of transition in plane Couette flow. *J. Fluid Mech.* **650**, 119–129.
DULLERUD, G.E. & LALL, S. 2002 A new approach for analysis and synthesis of time-varying systems. *IEEE Trans. Autom. Control* **44** (8), 1486–1497.
ELOFSSON, P.A. & ALFREDSSON, P.H. 2000 An experimental study of oblique transition in a Blasius boundary layer flow. *Eur. J. Mech. B/Fluids* **19** (5), 615–636.
FARANO, M., CHERUBINI, S., ROBINET, J.-C. & DE PALMA, P. 2015 Hairpin-like optimal perturbations in plane Poiseuille flow. *J. Fluid Mech.* **775**, R2.
FARRELL, B.F. & IOANNOU, P.J. 1993 Stochastic forcing of the linearized Navier–Stokes equations. *Phys. Fluids A* **5** (11), 2600–2609.
FRANK-SHAPIR, O. & GLUZMAN, I. 2025 Choosing between active and passive flow control via input–output analysis: application to Couette flow. *IEEE Control Syst. Lett.* **9**, 715–720.
FRANSSON, J.H.M., BRANDT, L., TALAMELLI, A. & COSSU, C. 2005 Experimental study of the stabilization of Tollmien–Schlichting waves by finite amplitude streaks. *Phys. Fluids* **17** (5), 054110.
GLUZMAN, I. & GAYME, D.F. 2021 Input–output framework for actuated boundary layers. *Phys. Rev. Fluids* **6**, 053901.
HE, S. & SEDDIGHI, M. 2015 Transition of transient channel flow after a change in Reynolds number. *J. Fluid Mech.* **764**, 395–427.
HEIDE, A.L. & HEMATI, M.S. 2025 Optimization framework for analyzing nonlinear stability due to sparse finite-amplitude perturbations. *Phys. Rev. Fluids* **10** (1), 014401.
HERNON, D., WALSH, E.J. & MCELIGOT, D.M. 2007 Experimental investigation into the routes to bypass transition and the shear-sheltering phenomenon. *J. Fluid Mech.* **591**, 461–479.
HUANG, Z., GAO, R., GAO, Y.Y. & XI, G. 2024 Subcritical transitional flow in two-dimensional plane Poiseuille flow. *J. Fluid Mech.* **994**, A6.
HWANG, Y. & COSSU, C. 2010*a* Amplification of coherent streaks in the turbulent Couette flow: an input–output analysis at low Reynolds number. *J. Fluid Mech.* **643**, 333–348.
HWANG, Y. & COSSU, C. 2010*b* Linear non-normal energy amplification of harmonic and stochastic forcing in the turbulent channel flow. *J. Fluid Mech.* **664**, 51–73.
JACOBS, R.G. & DURBIN, P.A. 2001 Simulations of bypass transition. *J. Fluid Mech.* **428**, 185–212.
JIN, B., SYMON, S. & ILLINGWORTH, S.J. 2021 Energy transfer mechanisms and resolvent analysis in the cylinder wake. *Phys. Rev. Fluids* **6** (2), 024702.
JOVANOVIC, M. & BAMIEH, B. 2001 The spatio-temporal impulse response of the linearized Navier–Stokes equations. In *Proceedings of the 2001 American Control Conference*, vol. 3, pp. 1948–1953. IEEE. (Cat. No. 01CH37148).
JOVANOVIC, M.R. 2004 *Modeling, Analysis, and Control of Spatially Distributed Systems*. University of California.
JOVANOVIĆ, MIHAILO R. 2021 From bypass transition to flow control and data-driven turbulence modeling: an input–output viewpoint. *Annu. Rev. Fluid Mech.*. **53**, 311–345.
JOVANOVIĆ, M.R. & BAMIEH, B. 2004 Unstable modes versus non-normal modes in supercritical channel flows. In *Proceedings of the 2004 American Control Conference*, vol. 3, pp. 2245–2250. IEEE.
JOVANOVIĆ, M.R. & BAMIEH, B. 2005 Componentwise energy amplification in channel flows. *J. Fluid Mech.* **534**, 145–183.
KALUR, A., MUSHTAQ, T., SEILER, P. & HEMATI, M.S. 2021*a* Estimating regions of attraction for transitional flows using quadratic constraints. *IEEE Control Syst. Lett.* **6**, 482–487.
KALUR, A., SEILER, P. & HEMATI, M.S. 2021*b* Nonlinear stability analysis of transitional flows using quadratic constraints. *Phys. Rev. Fluids* **6** (4), 044401.
KALUR, A., SEILER, P.J. & HEMATI, M. 2020 Stability and performance analysis of nonlinear and non-normal systems using quadratic constraints. In *AIAA Scitech 2020 Forum*, *AIAA Paper* 2020-0833. AIAA.
KARP, M. & COHEN, J. 2017 On the secondary instabilities of transient growth in Couette flow. *J. Fluid Mech.* **813**, 528–557.
KERSWELL, R.R. 2018 Nonlinear non-modal stability theory. *Annu. Rev. Fluid Mech.* **50** (1), 319–345.
KIM, J., MOIN, P. & MOSER, R. 1987 Turbulence statistics in fully developed channel flow at low Reynolds number. *J. Fluid Mech.* **177**, 133–166.
KLEBANOFF, P.S., TIDSTROM, K.D. & SARGENT, L.M. 1962 The three-dimensional nature of boundary-layer instability. *J. Fluid Mech.* **12** (1), 1–34.
KLOTZ, L., LEMOULT, G., FRONTCZAK, I., TUCKERMAN, L.S. & WESFREID, J.E. 2017 Couette–Poiseuille flow experiment with zero mean advection velocity: subcritical transition to turbulence. *Phys. Rev. Fluids* **2** (4), 043904.
KO, J., LUCOR, D. & SAGAUT, P. 2011 Effects of base flow uncertainty on Couette flow stability. *Comput. Fluids* **43** (1), 82–89.

https://doi.org/10.1017/jfm.2026.11214 Published online by Cambridge University Press

KREISS, G., LUNDBLADH, A. & HENNINGSON, D.S. 1994 Bounds for threshold amplitudes in subcritical shear flows. *J. Fluid Mech.* **270**, 175–198.
LAURIEN, E. & KLEISER, L. 1989 Numerical simulation of boundary-layer transition and transition control. *J. Fluid Mech.* **199**, 403–440.
LIU, C. & GAYME, D.F. 2020*a* An input–output based analysis of convective velocity in turbulent channels. *J. Fluid Mech.* **888**, A32.
LIU, C. & GAYME, D.F. 2020*b* Input–output inspired method for permissible perturbation amplitude of transitional wall-bounded shear flows. *Phys. Rev. E* **102** (6), 063108.
LIU, C. & GAYME, D.F. 2021 Structured input–output analysis of transitional wall-bounded flows. *J. Fluid Mech.* **927**, A25.
LIU, C., GLUZMAN, I., LOZIER, M., MIDYA, S., GORDEYEV, S., THOMAS, F.O. & GAYME, D.F. 2022 Spatial input–output analysis of actuated turbulent boundary layers. *AIAA J.* **60** (11), 6313–6327.
LOZANO-DURÁN, A., CONSTANTINOU, N.C., NIKOLAIDIS, M.-A. & KARP, M. 2021 Cause-and-effect of linear mechanisms sustaining wall turbulence. *J. Fluid Mech.* **914**, A8.
MADHUSUDANAN, A., ILLINGWORTH, S.J. & MARUSIC, I. 2019 Coherent large-scale structures from the linearized Navier–Stokes equations. *J. Fluid Mech.* **873**, 89–109.
MCKEON, B.J. 2017 The engine behind (wall) turbulence: perspectives on scale interactions. *J. Fluid Mech.* **817**, P1.
MCKEON, B.J., SHARMA, A.S. & JACOBI, I. 2013 Experimental manipulation of wall turbulence: a systems approach. *Phys. Fluids* **25** (3), 031301.
MCKEON, B.J. & SHARMA, A.S. 2010 A critical-layer framework for turbulent pipe flow. *J. Fluid Mech.* **658**, 336–382.
MULLIN, T. 2010 The rich structure of transition in a shear flow. *J. Fluid Mech.* **648**, 1–4.
MUSHTAQ, T., BHATTACHARJEE, D., SEILER, P. & HEMATI, M.S. 2024 Structured singular value of a repeated complex full-block uncertainty. *Intl J. Robust Nonlinear Control* **34** (7), 4881–4897.
MUSHTAQ, T., BHATTACHARJEE, D., SEILER, P.J. & HEMATI, M. 2023 Structured input–output tools for modal analysis of a transitional channel flow. In *AIAA SCITECH 2023 Forum*, *AIAA Paper* 2023-1805. AIAA.
NISHIOKA, M. & ASAI, M. 1985 Some observations of the subcritical transition in plane Poiseuille flow. *J. Fluid Mech.* **150**, 441–450.
NISHIOKA, M., *et al.* 1975 An experimental investigation of the stability of plane Poiseuille flow. *J. Fluid Mech.* **72** (4), 731–751.
ORSZAG, S.A. 1971 Accurate solution of the Orr–Sommerfeld stability equation. *J. Fluid Mech.* **50** (4), 689–703.
PACKARD, A. & DOYLE, J. 1993 The complex structured singular value. *Automatica* **29** (1), 71–109.
PARENTE, E., ROBINET, J.-C., DE PALMA, P. & CHERUBINI, S. 2022 Minimal energy thresholds for sustained turbulent bands in channel flow. *J. Fluid Mech.* **942**, A18.
PEIXINHO, J. & MULLIN, T. 2007 Finite-amplitude thresholds for transition in pipe flow. *J. Fluid Mech.* **582**, 169–178.
PFENNINGER, W. 1961 Transition in the inlet length of tubes at high Reynolds numbers. In *Boundary Layer and Flow Control: Its Principles and Application* (ed. G.V. Lachmann), vol. 2, pp. 970–980. Pergamon Press.
PHILIP, J., SVIZHER, A. & COHEN, J. 2007 Scaling law for a subcritical transition in plane Poiseuille flow. *Phys. Rev. Lett.* **98** (15), 154502.
PRIGENT, A., GRÉGOIRE, G., CHATÉ, H. & DAUCHOT, O. 2003 Long-wavelength modulation of turbulent shear flows. *Physica D* **174** (1–4), 100–113.
REDDY, S.C. & HENNINGSON, D.S. 1993 Energy growth in viscous channel flows. *J. Fluid Mech.* **252**, 209–238.
REDDY, S.C., SCHMID, P.J., BAGGETT, J.S. & HENNINGSON, D.S. 1998 On stability of streamwise streaks and transition thresholds in plane channel flows. *J. Fluid Mech.* **365**, 269–303.
RIST, U. & FASEL, H. 1995 Direct numerical simulation of controlled transition in a flat-plate boundary layer. *J. Fluid Mech.* **298**, 211–248.
ROACH, P.E. & BRIERLEY, D.H. 1989 The influence of a turbulent freestream on zero pressure gradient transitional boundary layer development. In *Numerical Simulation of Unsteady Flowsand Transition to Turbulence* (ed. O. Pironneau). Cambridge University Press.
ROMANOV, V.A. 1973 Stability of plane-parallel Couette flow. *Funct. Anal. Applics.* **7** (2), 137–146.
SANO, M. & TAMAI, K. 2016 A universal transition to turbulence in channel flow. *Nat. Phys.* **12** (3), 249–253.
SCHERER, C. 2001 *Theory of Robust Control*, pp. 1–160. Delft University of Technology.
SCHLICHTING, H. & GERSTEN, K. 2016 *Boundary-Layer Theory*. Springer.

https://doi.org/10.1017/jfm.2026.11214 Published online by Cambridge University Press

SCHMID, P.J. 2000 Linear stability theory and bypass transition in shear flows. *Phys. Plasmas* **7** (5), 1788–1794.

SCHMID, P.J. 2007 Nonmodal stability theory. *Annu. Rev. Fluid Mech.* **39** (1), 129–162.

SCHMID, P.J. & HENNINGSON, D.S. 1994 Optimal energy density growth in Hagen–Poiseuille flow. *J. Fluid Mech.* **277**, 197–225.

SCHMID, P.J., HENNINGSON, D.S. & JANKOWSKI, D.F. 2002 Stability and transition in shear flows. Applied mathematical sciences, vol. 142. *Appl. Mech. Rev.* **55** (3), B57–B59.

SHUAI, Y., LIU, C. & GAYME, D.F. 2023 Structured input–output analysis of oblique laminar–turbulent patterns in plane Couette–Poiseuille flow. *Intl J. Heat Fluid Flow* **103**, 109207.

SYMON, S., ILLINGWORTH, S.J. & MARUSIC, I. 2021 Energy transfer in turbulent channel flows and implications for resolvent modelling. *J. Fluid Mech.* **911**, A3.

TAIRA, K., HEMATI, M.S., BRUNTON, S.L., SUN, Y., DURAISAMY, K., BAGHERI, S., DAWSON, S.T.M. & YEH, C.-A. 2020 Modal analysis of fluid flows: applications and outlook. *AIAA J.* **58** (3), 998–1022.

TILLMARK, N. & ALFREDSSON, P.H. 1992 Experiments on transition in plane Couette flow. *J. Fluid Mech.* **235**, 89–102.

TREFETHEN, L.N. 2000 *Spectral Methods in MATLAB*. SIAM.

VAVALIARIS, C., BENEITEZ, M. & HENNINGSON, D.S. 2020 Optimal perturbations and transition energy thresholds in boundary layer shear flows. *Phys. Rev. Fluids* **5** (6), 062401.

WEIDEMAN, J.A. & REDDY, S.C. 2000 A MATLAB differentiation matrix suite. *ACM Trans. Math. Softw. (TOMS)* **26** (4), 465–519.

ZHOU, K., DOYLE, J.C. & GLOVER, K. 1995 *Robust and Optimal Control*. Pearson.

https://doi.org/10.1017/jfm.2026.11214 Published online by Cambridge University Press